

# UC Berkeley

## UC Berkeley Previously Published Works

### Title

Water Enables Efficient CO<sub>2</sub> Capture from Natural Gas Flue Emissions in an Oxidation-Resistant Diamine-Appended Metal–Organic Framework

### Permalink

<https://escholarship.org/uc/item/08n6p340>

### Journal

Journal of the American Chemical Society, 141(33)

### ISSN

0002-7863

### Authors

Siegelman, Rebecca L  
Milner, Phillip J  
Forse, Alexander C  
[et al.](#)

### Publication Date

2019-08-21

### DOI

10.1021/jacs.9b05567

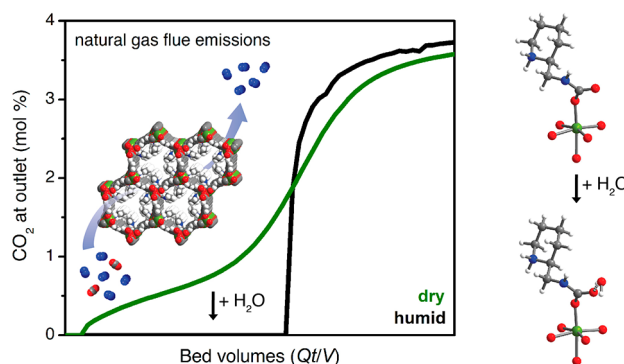
Peer reviewed

# Water Enables Efficient CO<sub>2</sub> Capture from Natural Gas Flue Emissions in an Oxidation-Resistant Diamine-Appended Metal–Organic Framework

Rebecca L. Siegelman,<sup>†,‡,¶,||</sup> Phillip J. Milner,<sup>†,‡,¶,||,◆</sup> Alexander C. Forse,<sup>†,‡,§,Ⓢ</sup> Jung-Hoon Lee,<sup>||,#</sup> Kristen A. Colwell,<sup>§</sup> Jeffrey B. Neaton,<sup>||,#,▽</sup> Jeffrey A. Reimer,<sup>§,‡,Ⓢ</sup> Simon C. Weston,<sup>○,Ⓢ</sup> and Jeffrey R. Long<sup>\*,†,§,‡,Ⓢ</sup>

<sup>†</sup>Department of Chemistry, <sup>‡</sup>Berkeley Energy and Climate Institute, <sup>§</sup>Department of Chemical and Biomolecular Engineering, and <sup>||</sup>Department of Physics, University of California, Berkeley, California 94720, United States  
<sup>‡</sup>Materials Sciences Division and <sup>#</sup>Molecular Foundry, Lawrence Berkeley National Laboratory, Berkeley, California 94720, United States  
<sup>▽</sup>Kavli Energy Nanosciences Institute at Berkeley, Berkeley, California 94720, United States  
<sup>○</sup>Corporate Strategic Research, ExxonMobil Research and Engineering Company, Annandale, New Jersey 08801, United States

**ABSTRACT:** Supported by increasingly available reserves, natural gas is achieving greater adoption as a cleaner-burning alternative to coal in the power sector. As a result, carbon capture and sequestration from natural gas-fired power plants is an attractive strategy to mitigate global anthropogenic CO<sub>2</sub> emissions. However, the separation of CO<sub>2</sub> from other components in the flue streams of gas-fired power plants is particularly challenging due to the low CO<sub>2</sub> partial pressure (~40 mbar), which necessitates that candidate separation materials bind CO<sub>2</sub> strongly at low partial pressures (≤4 mbar) to capture ≥90% of the emitted CO<sub>2</sub>. High partial pressures of O<sub>2</sub> (120 mbar) and water (80 mbar) in these flue streams have also presented significant barriers to the deployment of new technologies for CO<sub>2</sub> capture from gas-fired power plants. Here, we demonstrate that functionalization of the metal–organic framework Mg<sub>2</sub>(dobpdc) (dobpdc<sup>4-</sup> = 4,4'-dioxidobiphenyl-3,3'-dicarboxylate) with the cyclic diamine 2-(aminomethyl)piperidine (2-ampd) produces an adsorbent that is capable of ≥90% CO<sub>2</sub> capture from a humid natural gas flue emission stream, as confirmed by breakthrough measurements. This material captures CO<sub>2</sub> by a cooperative mechanism that enables access to a large CO<sub>2</sub> cycling capacity with a small temperature swing (2.4 mmol CO<sub>2</sub>/g with ΔT ≥ 100 °C). Significantly, multicomponent adsorption experiments, infrared spectroscopy, magic angle spinning solid-state NMR spectroscopy, and van der Waals-corrected density functional theory studies suggest that water enhances CO<sub>2</sub> capture in 2-ampd–Mg<sub>2</sub>(dobpdc) through hydrogen-bonding interactions with the carbamate groups of the ammonium carbamate chains formed upon CO<sub>2</sub> adsorption, thereby increasing the thermodynamic driving force for CO<sub>2</sub> binding. In light of the exceptional thermal and oxidative stability of 2-ampd–Mg<sub>2</sub>(dobpdc), its high CO<sub>2</sub> adsorption capacity, and its high CO<sub>2</sub> capture rate from a simulated natural gas flue emission stream, this material is one of the most promising adsorbents to date for this important separation.



## INTRODUCTION

The combustion of fossil fuels in the energy sector is currently responsible for the release of 32 Gt/year of CO<sub>2</sub> into the atmosphere, or approximately 65% of annual anthropogenic greenhouse gas emissions.<sup>1,2</sup> To limit the contribution of these emissions to global climate change, mitigation strategies are needed during the transition to cleaner fuel sources.<sup>2</sup> One of the most widely studied emission mitigation strategies is postcombustion carbon capture and sequestration (CCS), in which CO<sub>2</sub> is selectively removed from the flue gas streams of

fossil fuel- or biomass-fired power plants and sequestered underground.<sup>1–4</sup> To date, the large majority of efforts toward implementing CCS have focused on coal-fired power plants, which are currently responsible for approximately 45% of energy-related CO<sub>2</sub> emissions.<sup>4,5</sup> However, global consumption of natural gas has been increasing steadily, and its contribution to global primary energy is anticipated to overtake

56 that of coal by 2040 (New Policy Scenario, International  
57 Energy Agency).<sup>6</sup> Furthermore, in economies where natural  
58 gas is prevalent, such as that of the United States, the rapid  
59 transition away from coal has resulted in CO<sub>2</sub> emissions from  
60 the combustion of natural gas already exceeding those from  
61 coal, despite the fact that natural gas emits approximately half  
62 as much CO<sub>2</sub> as coal per unit electricity produced.<sup>7</sup> Therefore,  
63 new materials are urgently needed for the selective removal of  
64 CO<sub>2</sub> from the emissions of natural gas-fired power plants.<sup>8–10</sup>

65 The flue gas stream produced at a natural gas combined  
66 cycle (NGCC) power plant consists of approximately 74.4%  
67 N<sub>2</sub>, 12.4% O<sub>2</sub>, 8.4% H<sub>2</sub>O, 3.9% CO<sub>2</sub>, and 0.9% Ar.<sup>11</sup>  
68 Importantly, emissions from NGCC plants contain fewer  
69 pollutants than emission streams from coal-fired plants, which  
70 release SO<sub>x</sub>, NO<sub>x</sub>, heavy metals, and particulate matter.<sup>11</sup>  
71 These contaminants pose environmental hazards and serve as  
72 significant barriers to the deployment of CCS systems in coal-  
73 fired plants, particularly due to the known poisoning of a  
74 number of CO<sub>2</sub> capture materials by SO<sub>x</sub> and NO<sub>x</sub>.<sup>12–19</sup> The  
75 CO<sub>2</sub> partial pressure of NGCC flue gas (~40 mbar) is also  
76 significantly lower than that of coal flue gas (~150 mbar).<sup>11</sup> As  
77 a result, gas-fired plants are cleaner-burning than coal-fired  
78 plants, but CO<sub>2</sub> capture from the emissions of these power  
79 stations is more technically challenging. Specifically, the U.S.  
80 Department of Energy (DoE) has set a target of 90% capture  
81 of CO<sub>2</sub> from the emission stream,<sup>11</sup> requiring that candidate  
82 CO<sub>2</sub> capture materials bind CO<sub>2</sub> at concentrations as low as  
83 0.4%. Materials that meet this requirement often possess high  
84 CO<sub>2</sub> adsorption enthalpies,<sup>20</sup> necessitating energy-intensive  
85 cycling conditions and generating a potential trade-off between  
86 heat management and CO<sub>2</sub> cycling capacity.<sup>21</sup>

87 Owing to decades of development, aqueous amine solutions  
88 are the most technology-ready systems for large-scale CO<sub>2</sub>  
89 capture applications.<sup>22,23</sup> However, amine solutions face  
90 technological barriers to deployment for CO<sub>2</sub> capture from  
91 NGCC power plants due to their high regeneration energy  
92 costs and susceptibility to oxidative and thermal degrada-  
93 tion.<sup>24–27</sup> As an alternative, solid adsorbents, such as zeolites,  
94 amine-functionalized silicas, porous organic networks, and  
95 metal–organic frameworks, may offer enhanced stability,  
96 greater CO<sub>2</sub> cycling capacities, and inherently lower regener-  
97 ation energies.<sup>4,28–40</sup> Despite the flourishing research areas of  
98 adsorptive CO<sub>2</sub> capture from coal flue gas and air, only a  
99 handful of reports have yet explored adsorbent design  
100 specifically for CCS from gas-fired power plants.<sup>36,41–48</sup>  
101 More research is also needed to design adsorbents with high  
102 thermal and oxidative stabilities that can capture CO<sub>2</sub>  
103 selectively under humid conditions.

104 Recently, we<sup>49–53</sup> and others<sup>45,54–58</sup> have demonstrated the  
105 potential of diamine-appended variants of the metal–organic  
106 framework Mg<sub>2</sub>(dobpdc) (dobpdc<sup>4-</sup> = 4,4'-dioxidobiphenyl-  
107 3,3'-dicarboxylate) as transformative materials for carbon  
108 capture applications.<sup>59</sup> The unique step-shaped adsorption  
109 profiles of these frameworks enable cycling of the full CO<sub>2</sub>  
110 adsorption capacity with minimal temperature swings. We have  
111 further shown that the adsorption step of these materials can  
112 be tuned postsynthetically by changing the appended  
113 diamine,<sup>51</sup> a strategy that we employed to optimize an  
114 adsorbent for CO<sub>2</sub> capture from coal flue gas.<sup>52</sup> Our previous  
115 work posited that *primary*, *secondary* (1°/2°) diamine-  
116 appended variants of Mg<sub>2</sub>(dobpdc) are likely the most  
117 promising for CO<sub>2</sub> capture from NGCC flue gas, on the  
118 basis of their low CO<sub>2</sub> adsorption step pressures (<1 mbar at

40 °C) and minimal hysteresis upon CO<sub>2</sub> desorption.<sup>51</sup>  
119 However, these materials possess a trade-off between thermal  
120 stability and CO<sub>2</sub> adsorption capacity. Specifically, the largest  
121 1°/2° diamines were the most resistant to amine volatilization  
122 during temperature-swing cycling but also underwent a steric  
123 rearrangement at half saturation (0.5 CO<sub>2</sub> per diamine), which  
124 led to double-stepped CO<sub>2</sub> adsorption profiles.<sup>53</sup> As a result, at  
125 the low partial pressures relevant for NGCC CCS systems,  
126 only the capacity of the first CO<sub>2</sub> adsorption step (half of the  
127 theoretical capacity) would be accessible with such materials.  
128 While two similar base frameworks were shown to resolve the  
129 issue of steric crowding to enable single-step adsorption  
130 profiles with large diamines,<sup>53</sup> the initially studied  
131 Mg<sub>2</sub>(dobpdc)(diamine)<sub>2</sub> variants remain preferable due to  
132 their inexpensive components and favorable gravimetric  
133 (~3.5–4.0 mmol/g) and volumetric (~79–84 v/v) CO<sub>2</sub>  
134 adsorption capacities.<sup>51</sup> Additionally, Mg<sub>2</sub>(dobpdc) has already  
135 been prepared at the multikilogram scale,<sup>60</sup> facilitating rapid  
136 technology development.  
137

138 Herein, we demonstrate that appending the cyclic 1°/2°  
139 diamine 2-(aminomethyl)piperidine (2-ampd) to the metal  
140 sites in Mg<sub>2</sub>(dobpdc) alters the steric interactions and  
141 thermodynamics of CO<sub>2</sub> adsorption, giving rise to a material  
142 with two closely spaced adsorption steps. The adsorbent 2-  
143 ampd–Mg<sub>2</sub>(dobpdc) (Figure 1) is thermally stable and  
144 exhibits two CO<sub>2</sub> adsorption steps at pressures low enough  
145 to access the full chemisorptive capacity of the material (1 CO<sub>2</sub>  
146 per diamine) from NGCC flue gas. Importantly, we find that

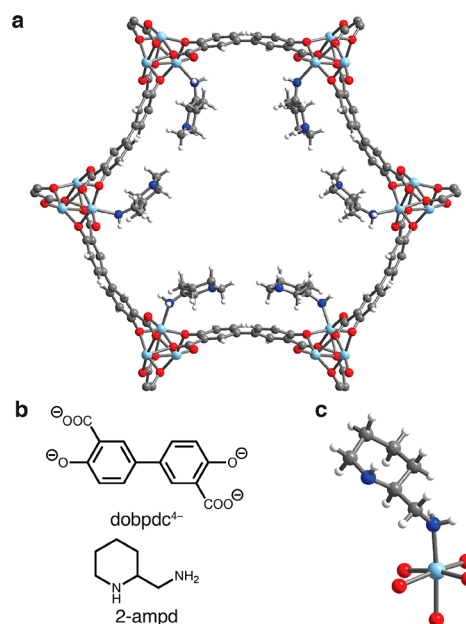


**Figure 1.** (a) Single-crystal X-ray diffraction structure of toluene-solvated 2-ampd–Zn<sub>2</sub>(dobpdc), which is isostructural to 2-ampd–Mg<sub>2</sub>(dobpdc). The left-handed diamine is depicted in the right-handed framework (space group *P*3<sub>1</sub>21). The structure was refined with a racemic mixture of 2-ampd in an inversion-twinned crystal. The enantiomeric diamine and toluene solvent molecules are omitted for clarity. (b) Chemical structures of the ligand dobpdc<sup>4-</sup> and the diamine 2-ampd. (c) First coordination sphere of the Zn(II) site depicting coordination of the left-handed enantiomer of 2-ampd. The diamines were found to coordinate exclusively through the primary amine. Light blue, blue, red, gray, and white spheres represent Zn, N, O, C, and H atoms, respectively.

147 the presence of water greatly improves the CO<sub>2</sub> adsorption  
 148 characteristics of this material, enabling it to achieve ≥90%  
 149 removal of CO<sub>2</sub> from simulated NGCC flue gas in break-  
 150 through measurements. While other amine-functionalized  
 151 adsorbents have shown improvements in CO<sub>2</sub> capture  
 152 performance due to a humidity-induced mechanistic shift,  
 153 our van der Waals (vdW)-corrected density functional theory  
 154 (DFT) calculations and spectroscopy measurements show that  
 155 the improved performance of 2-ampd–Mg<sub>2</sub>(dobpdc) under  
 156 humid conditions can instead be attributed to preferential  
 157 stabilization of the ammonium carbamate chains formed upon  
 158 CO<sub>2</sub> insertion. Our results demonstrate that 2-ampd–  
 159 Mg<sub>2</sub>(dobpdc) is among the most promising adsorbents  
 160 identified to date for this underexplored but extremely  
 161 important separation.

## 162 ■ EXPERIMENTAL SECTION

163 **General Procedures.** <sup>1</sup>H NMR spectra were collected on a  
 164 Bruker AMX 300 MHz spectrometer and referenced to residual  
 165 dimethyl sulfoxide ( $\delta = 2.50$  ppm). Powder X-ray diffraction (PXRD)  
 166 patterns were collected with a laboratory Bruker AXS D8 Advance  
 167 diffractometer with Cu K $\alpha$  radiation ( $\lambda = 1.5418$  Å) or at the  
 168 Advanced Photon Source with synchrotron radiation ( $\lambda = 0.45399$  Å),  
 169 as specified in the figure captions. Additional details for synchrotron  
 170 PXRD experiments under controlled atmospheres are given in  
 171 Supporting Information (SI) Section S15. All synthetic manipulations  
 172 were carried out under air unless noted otherwise. All solvents and  
 173 reagents, including diamines, were purchased from commercial  
 174 sources and used without further purification unless otherwise  
 175 noted. The linker H<sub>4</sub> dobpdc was purchased from Hangzhou Trylead  
 176 Chemical Technology Co. The linker H<sub>4</sub> dotpdc was prepared  
 177 according to the literature procedure.<sup>53</sup> The metal–organic frame-  
 178 works Mg<sub>2</sub>(dobpdc),<sup>51</sup> Mn<sub>2</sub>(dobpdc),<sup>52</sup> Ni<sub>2</sub>(dobpdc),<sup>52</sup>  
 179 Co<sub>2</sub>(dobpdc),<sup>52</sup> Zn<sub>2</sub>(dobpdc),<sup>61</sup> and Mg<sub>2</sub>(dotpdc)<sup>53</sup> were prepared  
 180 according to literature procedures (SI Section S1). Ultrahigh purity  
 181 (>99.998%) gases were used for all adsorption experiments.

182 **Infrared Spectra.** Attenuated total reflectance (ATR) infrared  
 183 (IR) spectra were collected on a PerkinElmer Spectrum 400 Fourier  
 184 Transform (FT) IR spectrometer equipped with a Pike GladiATR and  
 185 a home-built glovebag accessory used to control the atmosphere.  
 186 Three vacuum–refill cycles were used to exchange the atmosphere of  
 187 the glovebag accessory when preparing the system for in situ  
 188 experiments. For humid FTIR spectra, samples were placed in 4 mL  
 189 vials and sealed in a 20 mL vapor-dosing chamber containing ~4 mL  
 190 of water. After at least 15 min of equilibration, the powder was  
 191 removed, and spectra were collected. Co-adsorption of water in the  
 192 sample was confirmed by observation of the H<sub>2</sub>O IR vibrational bands  
 193 at 1638 and 3350 (broad) cm<sup>-1</sup>.<sup>62</sup>

194 **Diamine Grafting Procedure.**<sup>51</sup> A 20 mL scintillation vial was  
 195 charged with toluene (4 mL) and 2-ampd (1 mL). Methanol-solvated  
 196 Mg<sub>2</sub>(dobpdc) (~15 mg) was filtered and washed with toluene (2 ×  
 197 10 mL). (Note: Mg<sub>2</sub>(dobpdc) should not be allowed to dry  
 198 completely in air due to potential decomposition.<sup>49</sup>) The filter-dried  
 199 Mg<sub>2</sub>(dobpdc) was added to the diamine solution, and the vial was  
 200 swirled several times and allowed to stand at room temperature for at  
 201 least 12 h. After this time, the mixture was filtered, and the resulting  
 202 powder was washed with toluene (3 × 20 mL) and allowed to dry for  
 203 ~3 min under reduced pressure, yielding ~25 mg of toluene-solvated  
 204 2-ampd–Mg<sub>2</sub>(dobpdc). Other diamine-appended metal–organic  
 205 frameworks described in this work were prepared using a similar  
 206 procedure. Full characterization of all new diamine-appended  
 207 frameworks prepared as part of this work, including PXRD patterns,  
 208 IR spectra, dry N<sub>2</sub> thermogravimetric decomposition profiles, and  
 209 CO<sub>2</sub> adsorption/desorption isobars, are included in the SI. Diamine  
 210 loadings were determined by suspending ~5 mg of the diamine-  
 211 appended metal–organic framework in 0.5 mL of DMSO-*d*<sub>6</sub> and then  
 212 digesting the framework by adding several drops of DCl (35 wt % in  
 213 D<sub>2</sub>O) and heating until the mixture became homogeneous. The

214 resulting solutions were analyzed by <sup>1</sup>H NMR spectroscopy to  
 215 determine the ratio of diamine to organic linker. Representative  
 216 diamine loadings for all diamine-appended metal–organic frameworks  
 217 prepared as part of this work are included in the SI.

218 **Thermogravimetric Analysis and Cycling Measurements.**  
 219 Dry thermogravimetric analysis (TGA) experiments were conducted  
 220 using a TA Instruments TGA Q5000. Humid TGA experiments were  
 221 conducted using a TA Instruments TGA Q50. For humid experi-  
 222 ments, the incident gas stream was passed through two room-  
 223 temperature water bubblers in series, leading to an estimated water  
 224 content of 2.6%, as determined by comparison to the water isotherms  
 225 of 2-ampd–Mg<sub>2</sub>(dobpdc) (Figure S11). Premixed cylinders of CO<sub>2</sub> in  
 226 N<sub>2</sub> were obtained from Praxair. Samples were activated under flowing  
 227 N<sub>2</sub> for 20–30 min until the mass stabilized; exact activation  
 228 conditions for each diamine-appended material were determined  
 229 through careful analysis of the dry N<sub>2</sub> thermal decomposition profiles  
 230 and are included in the SI. Masses are uncorrected for buoyancy  
 231 effects. A flow rate of 25 mL/min was used for all TGA experiments.  
 232 Ramp rates for all isobaric measurements are included in figure  
 233 captions. A ramp rate of 1.5 °C/min was employed for all dry N<sub>2</sub>  
 234 decomposition experiments.

235 **Gas Adsorption Measurements.** Volumetric adsorption iso-  
 236 therms for N<sub>2</sub>, O<sub>2</sub>, and CO<sub>2</sub> were obtained using a Micromeritics  
 237 ASAP 2020 gas adsorption analyzer. Adsorption isotherms for water  
 238 were obtained using a Micromeritics 3Flex instrument. For water  
 239 isotherms, the stainless-steel vapor dosing apparatus was subjected to  
 240 three freeze–pump–thaw cycles to remove any dissolved gases, and  
 241 heat tape was used to keep the exposed portion of the glass sample  
 242 tube at elevated temperature to prevent condensation of water. The  
 243 maximum relative humidity accessible in measurements with water  
 244 was limited by the manifold temperature of 45 °C. Isotherms  
 245 collected at 40, 50, and 60 °C were measured using a circulating water  
 246 bath to control the sample temperature. Surface area measurements  
 247 with N<sub>2</sub> were carried out at 77 K using a liquid N<sub>2</sub> bath. Samples were  
 248 regenerated at 100 °C under reduced pressure (<10 μbar) for 2–4 h  
 249 between isotherms. The isotherm data points were considered  
 250 equilibrated after <0.01% change in pressure occurred over an  
 251 average of 11 intervals of 15 s (for N<sub>2</sub>, O<sub>2</sub>, and CO<sub>2</sub>) or 30 s (for  
 252 H<sub>2</sub>O).

253 **Calculation of Differential Enthalpies and Entropies of**  
 254 **Adsorption.** Using a linear spline interpolation method and the CO<sub>2</sub>  
 255 adsorption isotherms for 2-ampd–Mg<sub>2</sub>(dobpdc) (Figure S7), the  
 256 exact pressures ( $p_q$ ) corresponding to specific CO<sub>2</sub> loadings ( $q$ ) were  
 257 determined at different temperatures ( $T$ ). The Clausius–Clapeyron  
 258 relationship (eq 1) was used to calculate the differential enthalpies of  
 259 adsorption ( $\Delta h_{\text{ads}}$ ) based on the slopes of the linear trendlines fit to  
 260  $\ln(p_q)$  vs  $1/T$  (Figure S8). The  $y$ -intercepts of these linear trendlines  
 261 are equal to  $-\Delta s_{\text{ads}}/R$  at each loading (assuming  $p_0 = 1$  bar)<sup>63</sup> and  
 262 thus were used to determine the corresponding differential entropies  
 263 of adsorption (Figure S9).

$$\ln(p_q) = \left( \frac{\Delta h_{\text{ads}}}{R} \right) \left( \frac{1}{T} \right) + c \quad (1)$$

264 **Breakthrough Measurements.** See SI Section S11 for  
 265 experimental details and SI figures.

266 **Solid-State Magic Angle Spinning (MAS) NMR Experiments.**  
 267 Activation of 2-ampd–Mg<sub>2</sub>(dobpdc) was carried out under flowing  
 268 N<sub>2</sub> at 150 °C for 30 min. The activated material was packed into a 3.2  
 269 mm rotor inside a N<sub>2</sub>-filled glovebag and further activated under  
 270 vacuum inside a home-built gas manifold for 10 min at room  
 271 temperature. This manifold has the key feature of enabling gas dosing  
 272 of rotors at controlled pressures and subsequent sealing of dosed  
 273 rotors prior to removal from the manifold.<sup>61</sup> Samples were dosed with  
 274 <sup>13</sup>CO<sub>2</sub> gas (Sigma-Aldrich, 99 atom % <sup>13</sup>C, < 3 atom % <sup>18</sup>O) at room  
 275 temperature (~22 °C) and allowed to equilibrate for 30 min prior to  
 276 measurements, unless otherwise specified. For dosing with humid  
 277 CO<sub>2</sub>, a sample that had already been dosed with dry <sup>13</sup>CO<sub>2</sub> was  
 278 opened (the top and bottom rotor caps were removed), and the  
 279 sample was placed in a gas stream of humid CO<sub>2</sub> (relative humidity 280

281 ~70%, measured using a ThermoPro TP50 Hygrometer) that was  
 282 generated by flowing natural isotopic abundance CO<sub>2</sub> through a  
 283 bubbler containing deionized water for 1 h.

284 All solid-state NMR experiments were carried out at 16.4 T using a  
 285 Bruker 3.2 mm probe, and MAS rates were 15 kHz in all cases. All  
 286 solid-state <sup>13</sup>C NMR spectra were acquired by cross-polarization from  
 287 <sup>1</sup>H (<sup>15</sup>N and <sup>1</sup>H contact RF field strengths of 20 kHz and 35 kHz,  
 288 respectively). All cross-polarization experiments were acquired with  
 289 continuous wave <sup>1</sup>H decoupling at 82 kHz RF field strength, and with  
 290 the contact times stated in the figure captions. All <sup>1</sup>H NMR spectra  
 291 were acquired using a 90° pulse-acquire sequence with a RF field  
 292 strength of ~38 kHz, and recycle delays were adjusted to obtain  
 293 quantitative spectra. The <sup>1</sup>H, <sup>13</sup>C, and <sup>15</sup>N chemical shifts were  
 294 referenced to 1.8 ppm (adamantane), 38.5 ppm (adamantane tertiary  
 295 carbon, left-hand resonance), and 33.4 ppm (glycine), respectively.<sup>64</sup>

296 **Single-Crystal X-ray Diffraction.** Synthetic and experimental  
 297 details for single-crystal X-ray diffraction experiments with 2-ampd-  
 298 Zn<sub>2</sub>(dobpdc) and molecular 2-ampd-CO<sub>2</sub> are included in SI Sections  
 299 S12–S14.

300 **Density Functional Theory Calculations.** Our first-principles  
 301 DFT calculations used a plane-wave basis and projector augmented-  
 302 wave (PAW)<sup>65,66</sup> pseudopotentials with the Vienna ab initio  
 303 Simulation Package (VASP)<sup>67–70</sup> code. To include the effect of the  
 304 vdW dispersive interactions on binding energies and NMR chemical  
 305 shifts, we performed structural relaxations with vdW dispersion-  
 306 corrected functionals (vdW-DF2)<sup>71</sup> as implemented in VASP. For all  
 307 calculations, we used (i) a  $\Gamma$ -point sampling of the Brillouin zone  
 308 (except for NMR calculations, as specified below), (ii) a 1000 eV  
 309 plane-wave cutoff energy, and (iii) a 10<sup>-7</sup> eV self-consistency  
 310 criterion. We explicitly treat two valence electrons for Mg (3s<sup>2</sup>), six  
 311 for O (2s<sup>2</sup>2p<sup>4</sup>), five for N (2s<sup>2</sup>2p<sup>3</sup>), four for C (2s<sup>2</sup>2p<sup>2</sup>), and one for H  
 312 (1s<sup>1</sup>). All structural relaxations were performed with a Gaussian  
 313 smearing of 0.05 eV.<sup>72</sup> The ions were relaxed until the Hellmann-  
 314 Feynman forces were less than 0.001 eVÅ<sup>-1</sup>. To compute CO<sub>2</sub> and  
 315 H<sub>2</sub>O binding energies, we optimized the structure of 2-ampd-  
 316 Mg<sub>2</sub>(dobpdc) prior to CO<sub>2</sub> and H<sub>2</sub>O adsorption ( $E_{\text{ampd-MOF}}$ ),  
 317 interacting with CO<sub>2</sub> and H<sub>2</sub>O in the gas phase ( $E_{\text{CO}_2/\text{H}_2\text{O}}$ ) within  
 318 a 15 × 15 × 15 Å<sup>3</sup> cubic supercell, and 2-ampd-Mg<sub>2</sub>(dobpdc) with  
 319 adsorbed CO<sub>2</sub> and H<sub>2</sub>O molecules ( $E_{\text{CO}_2\text{-ampd-MOF}}$ ) using vdW-  
 320 corrected DFT. The binding energies ( $E_B$ ) were obtained via the  
 321 difference:

$$322 \quad E_B = E_{\text{CO}_2\text{-ampd-MOF}} - (E_{\text{ampd-MOF}} + E_{\text{CO}_2/\text{H}_2\text{O}}) \quad (2)$$

323 For NMR simulations, we used a 1 × 1 × 3 k-point. With this k-point,  
 324 the isotropic chemical shielding values ( $\delta_{\text{iso}}$ ) converged to 0.1 ppm.  
 325 Since the isotropic chemical shift ( $\delta_{\text{iso}}$ ) is obtained from  $\delta_{\text{iso}} = -(\delta_{\text{iso}} - \delta_{\text{ref}})$   
 326 where  $\delta_{\text{ref}}$  is a reference value, we needed to determine a  $\delta_{\text{ref}}$   
 327 value by comparing experimental  $\delta_{\text{iso}}$  values to calculated  $\delta_{\text{iso}}$  values.  
 328 The  $\sigma_{\text{ref}}$  values for <sup>1</sup>H (31.4 ppm) and <sup>13</sup>C (160.1 ppm) were  
 329 obtained by first computing  $\sigma_{\text{iso}}$  values for cocaine (CSD refcode  
 330 COCAIN10 was used as the starting point, and the structure was  
 331 geometry optimized before NMR calculation; see SI for coordinates).  
 332 The computed values were then compared with experimental values  
 333 (Table S18, Figure S94).<sup>73</sup> The  $\sigma_{\text{ref}}$  value for <sup>15</sup>N (215.9 ppm) was  
 334 determined by comparison of DFT-calculated  $\sigma_{\text{iso}}$  and the  
 335 experimental  $\delta_{\text{iso}}$  value for glycine (Table S18).<sup>61</sup> Additional DFT  
 336 figures and details are included in SI Section S21.

## 337 ■ RESULTS AND DISCUSSION

338 **Adsorbent Design for NGCC Post-Combustion Cap-**  
 339 **ture.** Our previous crystallographic and gas adsorption studies  
 340 of 1°, 2° diamine-appended Mg<sub>2</sub>(dobpdc) indicated that  
 341 unfavorable chain-chain interactions in the *ab* plane of the  
 342 framework give rise to the two-step adsorption profiles of these  
 343 materials.<sup>53</sup> We reasoned that tethering the alkyl chain to the  
 344 backbone of the diamine should alleviate these steric  
 345 interactions, thereby minimizing the gap between the two  
 346 CO<sub>2</sub> adsorption steps and enabling access to the full theoretical

adsorption capacity. Accordingly, we grafted racemic 2- 347  
 (aminomethyl)piperidine (2-ampd, Figure 1b) to 348  
 Mg<sub>2</sub>(dobpdc) using our previously reported procedure<sup>51</sup> to 349  
 produce the adsorbent 2-ampd-Mg<sub>2</sub>(dobpdc). Consistent 350  
 with our hypothesis, this material exhibits two closely spaced 351  
 steps in its CO<sub>2</sub> adsorption isotherms (occurring at 1.0 and 3.7 352  
 mbar at 40 °C, respectively; see Figure 2). Importantly, both 353 2

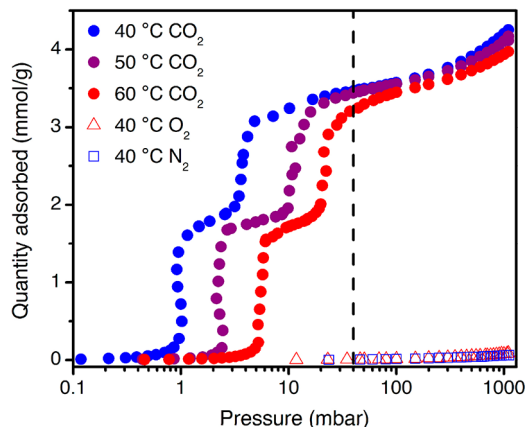


Figure 2. Pure CO<sub>2</sub> adsorption isotherms at 40, 50, and 60 °C (purple, blue, and red circles, respectively), and for O<sub>2</sub> (red triangles) and N<sub>2</sub> (blue squares) at 40 °C, for 2-ampd-Mg<sub>2</sub>(dobpdc). The dashed black line indicates the approximate partial pressure of CO<sub>2</sub> in flue gas from a NGCC power plant (40 mbar).

steps occur at pressures low enough to facilitate ≥90% removal 354  
 of CO<sub>2</sub> (residual pressure of ≤4 mbar) from NGCC flue 355  
 emissions under idealized, equilibrium conditions at 40 °C. In 356  
 contrast, variants of Mg<sub>2</sub>(dobpdc) functionalized with 357  
 diamines bearing long alkyl substituents, such as *N*-(*n*- 358  
 hexyl)ethylenediamine (*n*Hex-2),<sup>53</sup> have two widely spaced 359  
 CO<sub>2</sub> adsorption steps, restricting the quantity of CO<sub>2</sub> that can 360  
 be captured to the capacity of the lower-pressure step (~1.8 361  
 mmol/g at 40 mbar and 40 °C for *n*Hex-2, in contrast to 3.47 362  
 mmol/g for 2-ampd under the same conditions; Figure S16). 363

We hypothesize that step-shaped CO<sub>2</sub> adsorption in 2- 364  
 ampd-Mg<sub>2</sub>(dobpdc) arises as a result of cooperative insertion 365  
 of CO<sub>2</sub> into the metal-amine bonds to form chains of 366  
 ammonium carbamate running along the pore axis, as reported 367  
 previously for related alkylethylenediamine-appended frame- 368  
 works.<sup>49–58</sup> This conclusion is supported by spectroscopic 369  
 characterization (discussed below) and by the observed metal 370  
 dependence of the cooperative adsorption step position<sup>50</sup> for 371  
 2-ampd-M<sub>2</sub>(dobpdc) variants (M = Mg, Mn, Ni, Co, Zn; 372  
 Figure S85). In addition, appending 2-ampd within the 373  
 expanded terphenyl framework Mg<sub>2</sub>(dotpdc) (dotpdc<sup>4-</sup> = 374  
 4,4'-dioxido-[1,1':4',1''-terphenyl]-3,3''-dicarboxylate) produ- 375  
 ces an adsorbent with only one step in its CO<sub>2</sub> adsorption 376  
 isobar (Figure S21), confirming that the two adsorption steps 377  
 observed for 2-ampd-Mg<sub>2</sub>(dobpdc) also arise from steric 378  
 interactions between adjacent diamines in the framework (SI 379  
 Section S4). Importantly, 2-ampd-Mg<sub>2</sub>(dobpdc) possesses 380  
 comparable or superior thermal stability to all other 1°/2° 381  
 diamine-appended variants of Mg<sub>2</sub>(dobpdc) evaluated to date 382  
 (Figure S6), withstanding 12 h of exposure to flowing, humid 383  
 CO<sub>2</sub> at a regeneration temperature of 140 °C (or even as high 384  
 as 180 °C) with minimal diamine volatilization (Table S15, see 385  
 also discussion below). Therefore, the cyclic diamine 2-ampd 386  
 uniquely affords the best attributes achieved with 1°/2° 387

388 diamine-appended  $\text{Mg}_2(\text{dobpdc})$  materials to date, namely,  
389 high thermal stability coupled with a high  $\text{CO}_2$  adsorption  
390 capacity from a NGCC flue gas stream.

391 The single crystal X-ray diffraction structure of the  
392 isostructural framework 2-ampd- $\text{Zn}_2(\text{dobpdc})$  (Figure 1)  
393 provides insight into the thermal stability and close  $\text{CO}_2$   
394 adsorption steps of 2-ampd- $\text{Mg}_2(\text{dobpdc})$ . The bulky  
395 piperidine ring of 2-ampd can maintain a stable chair  
396 conformation in the pores of the framework, with efficient  
397 packing in the *ab* plane and minimization of unfavorable  
398 interactions between adjacent diamines. Consistently, despite  
399 the high density of amine groups within the pores, 2-ampd-  
400  $\text{Mg}_2(\text{dobpdc})$  exhibits a high Brunauer-Emmett-Teller  
401 surface area of  $618 \pm 2 \text{ m}^2/\text{g}$  (Figure S4), which should  
402 enable rapid diffusion of  $\text{CO}_2$  through the channels of the  
403 framework, even after  $\text{CO}_2$  adsorption.

404 **Single-Component Adsorption Experiments.** Follow-  
405 ing validation of these initial design criteria, we investigated  
406 additional properties relevant to the application of 2-ampd-  
407  $\text{Mg}_2(\text{dobpdc})$  in  $\text{CO}_2$  capture from NGCC flue emissions.  
408 Isothermal adsorption profiles were collected at 40, 50, and 60  
409  $^\circ\text{C}$  for  $\text{CO}_2$  and at 40  $^\circ\text{C}$  for  $\text{N}_2$  and  $\text{O}_2$  (Figure 2). For  $\text{CO}_2$ ,  
410 two adsorption steps were observed at all temperatures. Both  
411 adsorption steps occur below 40 mbar even at 60  $^\circ\text{C}$  and are  
412 predicted to be operative in this target pressure range up to  
413 approximately 69  $^\circ\text{C}$  (Figure S14). Importantly, because 2-  
414 ampd- $\text{Mg}_2(\text{dobpdc})$  adsorbs minimal  $\text{CO}_2$  at partial pressures  
415 beneath the first step pressure, processes with higher  
416 adsorption temperatures can be considered without sacrificing  
417  $\text{CO}_2$  adsorption capacity, as would be expected for a typical  
418 Langmuir-type adsorbent. Eliminating the need to adsorb at  
419 the lowest possible temperature can potentially reduce process  
420 costs through relaxed requirements for flue gas cooling,<sup>74</sup>  
421 minimization of water coadsorption,<sup>47</sup> and/or enhanced  
422 tolerance to temperature rise in the adsorbent bed upon  
423 exothermic  $\text{CO}_2$  adsorption.<sup>21</sup> In addition, despite demonstrat-  
424 ing strong adsorption of  $\text{CO}_2$  at low partial pressures, 2-ampd-  
425  $\text{Mg}_2(\text{dobpdc})$  can be fully regenerated by heating to only 140  
426  $^\circ\text{C}$  under a flow of dry or humid  $\text{CO}_2$  at atmospheric pressure  
427 (Figure S37). Furthermore, at the partial pressures relevant to  
428 natural gas flue emissions, 2-ampd- $\text{Mg}_2(\text{dobpdc})$  demon-  
429 strates excellent noncompetitive  $\text{CO}_2/\text{N}_2$  and  $\text{CO}_2/\text{O}_2$   
430 selectivities of 1320 and 694, respectively (Table S1), which  
431 are among the highest reported for a nonsize-selective metal-  
432 organic framework.<sup>31,35,75-78</sup> Because  $\text{N}_2$  and  $\text{O}_2$  cannot  
433 participate in the  $\text{CO}_2$ -selective cooperative adsorption  
434 mechanism, these values are anticipated to be reflective of  
435 the multicomponent performance of the material.

436 The thermodynamics of  $\text{CO}_2$  adsorption in 2-ampd-  
437  $\text{Mg}_2(\text{dobpdc})$  were analyzed using the data in Figure 2. A  
438 spline interpolation method was used to calculate lines of  
439 constant loading for the set of  $\text{CO}_2$  isotherms from 40 to 60  
440  $^\circ\text{C}$ . Employing the Clausius-Clapeyron relationship yielded a  
441 differential enthalpy of adsorption ( $\Delta h_{\text{ads}}$ ) of  $-73 \pm 2 \text{ kJ/mol}$   
442 at a loading of 1 mmol/g (Figure S8), similar to that observed  
443 for other diamine-appended variants of  $\text{Mg}_2(\text{dobpdc})$ <sup>50-52</sup> and  
444 smaller in magnitude than the low-coverage enthalpies  
445 reported for silicas functionalized with primary or secondary  
446 amines.<sup>79</sup> From this adsorption enthalpy, we calculated a  
447 projected regeneration energy of 2.8 MJ/kg  $\text{CO}_2$  for a  
448 temperature swing adsorption (TSA) process consisting of  
449 capture from a 40 mbar stream of  $\text{CO}_2$  at 40  $^\circ\text{C}$  and  
450 desorption under 1 bar of  $\text{CO}_2$  at 140  $^\circ\text{C}$  (see SI Section S3;

note that only  $\text{CO}_2$  was considered in this calculation). This  
451 value is over 30% lower than the regeneration energy projected  
452 for a polyamine-functionalized silica for a similar process (3.9  
453 MJ/kg  $\text{CO}_2$ , see SI Section S3),<sup>48</sup> reflecting the advantage of  
454 cooperative adsorbents for  $\text{CO}_2$  capture applications. Fur-  
455 thermore, with a higher adsorption temperature of 60  $^\circ\text{C}$ , an  
456 even lower projected regeneration energy of 2.7 MJ/kg  $\text{CO}_2$   
457 may be possible for 2-ampd- $\text{Mg}_2(\text{dobpdc})$  (considering only  
458  $\text{CO}_2$ ; see Table S2). Notably, the thermodynamics of  
459 adsorption for 2-ampd- $\text{Mg}_2(\text{dobpdc})$  were found to adhere  
460 to the same enthalpy-entropy correlation as other diamine-  
461 appended variants of  $\text{Mg}_2(\text{dobpdc})$ <sup>51</sup> (Figure S15), corrobo-  
462 rating the formation of ammonium carbamate chains upon  
463  $\text{CO}_2$  adsorption in this material.

464 **Mixed-Gas Adsorption Experiments.** While single-  
465 component equilibrium data are needed to guide adsorbent  
466 design and characterize fundamental adsorption properties,  
467 multicomponent experiments are critical to evaluate adsorbent  
468 performance under more realistic process conditions. To that  
469 end, we performed extensive dry and humid thermogravimetric  
470 experiments with 2-ampd- $\text{Mg}_2(\text{dobpdc})$  using  $\text{CO}_2/\text{N}_2$   
471 mixtures and simulated NGCC flue emission streams. When  
472 exposed to a flow of dry simulated NGCC flue gas (4%  $\text{CO}_2$  in  
473  $\text{N}_2$ ) at atmospheric pressure, 2-ampd- $\text{Mg}_2(\text{dobpdc})$  exhibits a  
474 high  $\text{CO}_2$  capacity of 16.0 g/100 g (3.63 mmol/g) at 40  $^\circ\text{C}$   
475 (Figure 3a, purple curve), consistent with the predicted  
476 capacity of 3.66 mmol/g for adsorption of 1  $\text{CO}_2$  per diamine.  
477 This adsorption capacity is significantly higher than that of  
478 other cyclic diamine-appended variants of  $\text{Mg}_2(\text{dobpdc})$   
479 (2.02-2.33 mmol/g, Figure S30), as well as the representative  
480 amine-functionalized silica MCM-41-PEI-50<sup>80,81</sup> (1.48 mmol/  
481 g, Figure S79) under equivalent conditions. However, for a dry  
482 0.4%  $\text{CO}_2$  in  $\text{N}_2$  stream, representing the lowest adsorption  
483 pressure (4 mbar  $\text{CO}_2$ ) required for 90% capture of  $\text{CO}_2$  from  
484 NGCC emissions, the adsorption capacity at 40  $^\circ\text{C}$  (2.81 g/  
485 100 g, or 0.639 mmol/g, Figure 3a) is significantly lower than  
486 that observed in the 40  $^\circ\text{C}$  pure  $\text{CO}_2$  isotherm at the same  
487  $\text{CO}_2$  partial pressure (2.76 mmol/g). Even with extremely slow  
488 isobaric cooling rates, similar discrepancies in the threshold  
489 conditions for cooperative adsorption have been observed  
490 between  $\text{CO}_2$  adsorption isobars (collected under flowing  
491  $\text{CO}_2/\text{N}_2$  mixtures) and volumetric isotherms (collected under  
492 pure  $\text{CO}_2$  starting from vacuum).<sup>82,83</sup> In general, the isobaric  
493 measurements show lower isobaric step temperatures (equiv-  
494 alent to higher isothermal step pressures) than would be  
495 expected given the measured equilibrium adsorption iso-  
496 therms. These results suggest a smaller thermodynamic driving  
497 force for  $\text{CO}_2$  capture under the more realistic, mixed-gas flow  
498 conditions. Additionally, we found that the adsorption capacity  
499 decreased when a faster cooling ramp rate (0.2 versus 0.1  $^\circ\text{C}/$   
500 min) was employed, suggesting that the adsorption kinetics are  
501 limited in streams with low  $\text{CO}_2$  partial pressures (SI Section  
502 S9). This result is consistent with a previous report  
503 investigating the adsorption kinetics of the related material  
504 mmen- $\text{Mg}_2(\text{dobpdc})$  (mmen = *N,N'*-dimethylethylenedi-  
505 amine).<sup>84</sup> Ultimately, thermodynamic and kinetic factors  
506 under process-relevant flow conditions indicate that 2-  
507 ampd- $\text{Mg}_2(\text{dobpdc})$  falls short of achieving the target of  
508  $\geq 90\%$   $\text{CO}_2$  capture from NGCC flue gas under *dry* conditions.

509 We also analyzed the ability of 2-ampd- $\text{Mg}_2(\text{dobpdc})$  to  
510 capture  $\text{CO}_2$  in the presence of water, which can constitute up  
511 to  $\sim 8\%$  of NGCC flue gas by volume. Humid isobars were  
512 collected by flowing  $\text{CO}_2/\text{N}_2$  mixtures through two room-  
513

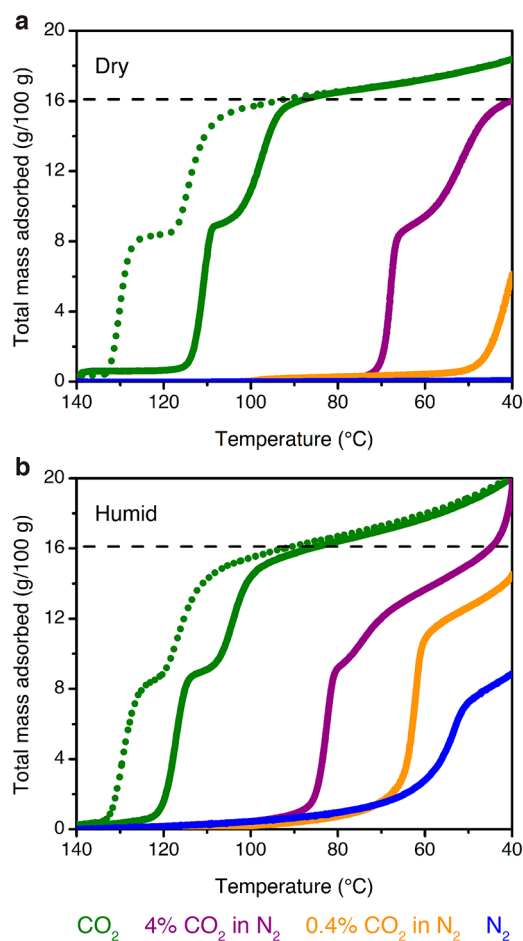


**Figure 3.** Dry (a) and humid (b,  $\sim 2.6\%$  H<sub>2</sub>O) isobars at atmospheric pressure for pure CO<sub>2</sub> (green), 4% CO<sub>2</sub> in N<sub>2</sub> (purple), 0.4% CO<sub>2</sub> in N<sub>2</sub> (orange), and pure N<sub>2</sub> (blue) in 2-ampd-Mg<sub>2</sub>(dobpdc). Solid lines depict adsorption (cooling), and dotted green lines depict desorption (heating) for the pure CO<sub>2</sub> isobars. The dashed black lines indicate the theoretical capacity for adsorption of 1 CO<sub>2</sub> per diamine. Temperature ramp rates: 0.5 °C/min for pure CO<sub>2</sub>, 0.1 °C/min for 4% and 0.4% CO<sub>2</sub> in N<sub>2</sub>, and 1 °C/min for pure N<sub>2</sub>.

514 temperature water bubblers to generate an estimated water  
 515 content of  $\sim 2.6$  vol % (Figure 3b; see Figures S37–S46 and  
 516 Tables S9 and S10 for direct comparisons of dry and humid  
 517 isobars). Importantly, the temperature of each CO<sub>2</sub> adsorption  
 518 step increased by 6 °C under humid conditions, with the step  
 519 inflection points shifting from 111 to 117 °C and from 98 to  
 520 104 °C (solid green curves, Figure 3). These higher adsorption  
 521 temperatures under humid conditions reflect thermodynamically  
 522 more favorable cooperative adsorption of CO<sub>2</sub> in the  
 523 presence of water. Likewise, under a flow of humid 4% CO<sub>2</sub>  
 524 (40 mbar) in N<sub>2</sub>, the inflection point of the higher-temperature  
 525 adsorption step increased by  $\sim 14$  °C, from 68 to 82 °C  
 526 (purple curves, Figure 3). Critically, while 2-ampd-  
 527 Mg<sub>2</sub>(dobpdc) captures limited CO<sub>2</sub> from a dry stream  
 528 containing 0.4% (4 mbar) CO<sub>2</sub> in N<sub>2</sub>, the addition of humidity  
 529 under the same conditions results in a sharp CO<sub>2</sub> step in the  
 530 adsorption isobar, with an inflection point at 64 °C (orange  
 531 curves, Figure 3). While the composition of the adsorbed  
 532 phase cannot be determined directly from these experiments, a  
 533 comparison of the humid CO<sub>2</sub>/N<sub>2</sub> mixture isobars with a  
 534 humid N<sub>2</sub> isobar indicates that the humid 0.4% CO<sub>2</sub> isobar  
 535 involves the adsorption of CO<sub>2</sub> (orange and blue curves,

Figure 3b). However, at lower temperatures, the saturation  
 536 capacities of the humid CO<sub>2</sub>/N<sub>2</sub> mixture isobars exceed the  
 537 gravimetric uptake anticipated for adsorption of 1 CO<sub>2</sub> per  
 538 diamine, suggesting coadsorption of water. In summary, the  
 539 isobaric adsorption data indicate that while 2-ampd-  
 540 Mg<sub>2</sub>(dobpdc) may fall below the target of  $\geq 90\%$  CO<sub>2</sub> capture  
 541 from dry NGCC flue emissions, the presence of humidity in  
 542 the gas stream should enable the material to reach this target at  
 543 temperatures up to at least 60 °C. 544

To quantify the influence of water on the thermodynamics  
 545 of CO<sub>2</sub> capture, approximate CO<sub>2</sub> adsorption enthalpies were  
 546 calculated for the dry and humid CO<sub>2</sub>/N<sub>2</sub> mixture isobars by  
 547 employing the Clausius–Clapeyron relationship at the  
 548 midpoint of each adsorption step. We note that while slow  
 549 temperature ramp rates were used to approximate equilibrium  
 550 conditions (SI Section S9), the enthalpies calculated from the  
 551 adsorption isobars were found to be systematically higher than  
 552 those calculated from the single-component, volumetric  
 553 isotherms. Nonetheless, the difference between the humid  
 554 and dry isobar enthalpies ( $\Delta h_{\text{ads,humid}} - \Delta h_{\text{ads,dry}}$ ) should reflect  
 555 the enthalpic benefit of CO<sub>2</sub> adsorption in the presence of  
 556 water. Using this method, we attribute the increased  
 557 temperature of the first adsorption step to a  $31 \pm 2$  kJ/mol  
 558 increase in the effective  $-\Delta h_{\text{ads}}$  in the presence of water (dry:  
 559  $81 \pm 1$  kJ/mol; humid:  $112 \pm 2$  kJ/mol). Notably, within  
 560 error, the same increase in effective  $-\Delta h_{\text{ads}}$  was found for the  
 561 lower-temperature adsorption step ( $30 \pm 2$  kJ/mol), indicating  
 562 that water uniformly increases the thermodynamic driving  
 563 force for both adsorption steps (Tables S7 and S8).  
 564 Interestingly, minimal change was observed in the isobaric  
 565 desorption step temperatures following saturation with CO<sub>2</sub>/  
 566 H<sub>2</sub>O under the tested humidity, resulting in calculation of  
 567 equivalent enthalpies within error (dry:  $101 \pm 1$  kJ/mol;  
 568 humid:  $99 \pm 1$  kJ/mol; difference:  $-2 \pm 2$  kJ/mol). While  
 569 these results are complicated by the lower relative humidities at  
 570 the elevated desorption temperatures, the similar dry and  
 571 humid CO<sub>2</sub> desorption step temperatures suggest that water  
 572 desorbs before CO<sub>2</sub>. 573

In order to quantify the influence of water on the  
 574 performance of 2-ampd-Mg<sub>2</sub>(dobpdc), we collected single-  
 575 component water adsorption isotherms at 30, 40, 50, and 60  
 576 °C. For all temperatures, the isotherms show a plateau at a  
 577 loading of 1 H<sub>2</sub>O per diamine, followed by condensation at  
 578 higher relative humidities (Figures S10 and S11). Using the  
 579 same spline interpolation method as for CO<sub>2</sub>, a differential  
 580 adsorption enthalpy of  $-65 \pm 2$  kJ/mol was calculated at a  
 581 loading of 1 mmol H<sub>2</sub>O/g (Figure S12). Assuming  
 582 coadsorption and desorption cycling of 1 water molecule per  
 583 diamine-Mg<sup>2+</sup> site alongside cycled CO<sub>2</sub>, the regeneration  
 584 energy of 2-ampd-Mg<sub>2</sub>(dobpdc) would increase by up to 1.5  
 585 MJ/kg CO<sub>2</sub> to a total of 4.3 MJ/kg CO<sub>2</sub> (SI Section S3). We  
 586 note that these values are only approximations, as they do not  
 587 account for potential differences in the adsorption enthalpy of  
 588 water on the CO<sub>2</sub>-inserted and diamine-bound phases (see  
 589 DFT calculations below), the potential effect of higher relative  
 590 humidity levels on adsorption or desorption, and the relative  
 591 adsorption/desorption kinetics of CO<sub>2</sub> vs H<sub>2</sub>O in the ultimate  
 592 cycling configuration. Nonetheless, 2-ampd-Mg<sub>2</sub>(dobpdc) is  
 593 still predicted to afford significant energy savings over  
 594 competing amine-based technologies such as a PEI-function-  
 595 alized silica, which requires a regeneration energy of 4.7 MJ/kg  
 596 CO<sub>2</sub> under similar conditions (SI Section S3)<sup>48</sup> and is  
 597 susceptible to degradative reaction pathways, such as urea  
 598

599 formation (Figures S74–S77, discussed in greater detail  
 600 below). Therefore, while these measurements indicate that  
 601 the presence of water in the incident gas stream improves the  
 602 thermodynamic driving force for CO<sub>2</sub> adsorption in 2-ampd–  
 603 Mg<sub>2</sub>(dobpdc), this improvement comes at the potential cost of  
 604 an increase in the regeneration energy associated with the  
 605 desorption of coadsorbed water. The cocycled water would  
 606 then need to be condensed prior to compression and transport  
 607 of the captured CO<sub>2</sub>.

608 **Fixed-Bed Adsorption Experiments.** To evaluate the  
 609 performance of 2-ampd–Mg<sub>2</sub>(dobpdc) in a fixed-bed  
 610 adsorption process, we conducted breakthrough experiments  
 611 under dry and humid simulated NGCC flue gas. These  
 612 experiments are particularly important for materials with step-  
 613 shaped isotherms, which often give rise to complex, multi-  
 614 modal breakthrough profiles. Such profiles were originally  
 615 anticipated for diamine-appended frameworks by Mazzotti and  
 616 co-workers in a comprehensive modeling study,<sup>45</sup> and a review  
 617 of the underlying theory is included in SI Section S10. In short,  
 618 the breakthrough profile can be predicted from an isotherm  
 619 with one or more inflection points by applying “Golden’s  
 620 Rule,” alternatively known as the rubber band rule or string  
 621 rule.<sup>45,85–87</sup> When applying this rule, an operating curve for  
 622 adsorption is constructed by stretching a hypothetical “rubber  
 623 band” beneath the adsorption isotherm from the initial state  
 624 (0% CO<sub>2</sub>) to the feed state (4% CO<sub>2</sub>). In concentration  
 625 regimes bounded by individual points of contact with the  
 626 rubber band, a compressive “shock” is anticipated in the  
 627 breakthrough profile. In concentration regimes where the  
 628 rubber band runs along the isotherm, a dispersive “wave” is  
 629 expected. With a step-shaped isotherm, the result is often a  
 630 “shock–wave–shock” profile: an initial “shock” is generated as  
 631 CO<sub>2</sub> slips through the bed at concentrations beneath the step,  
 632 followed by a “wave” corresponding to a small increase in CO<sub>2</sub>  
 633 concentration during the onset of the cooperative adsorption  
 634 step, and finally a second “shock” at full breakthrough (see  
 635 Figure S52). Intuitively, the shock–wave–shock profile can be  
 636 understood as a manifestation of the general inability of a  
 637 cooperative adsorbent to capture CO<sub>2</sub> once the CO<sub>2</sub> partial pressure  
 638 in the bed drops below the step pressure. Accordingly, this  
 639 behavior is the basis for our design criterion to achieve 90%  
 640 capture of CO<sub>2</sub> through the selection of adsorbents with step  
 641 pressures at <10% of the feed concentration.<sup>51</sup>

642 Breakthrough experiments were conducted with 0.73 g of  
 643 semispherical pellets of 2-ampd–Mg<sub>2</sub>(dobpdc) (350–700 μm)  
 644 under 28 sccm of 4% CO<sub>2</sub> in N<sub>2</sub> at 1.1 bar (Figure 4; details of  
 645 pellet preparation and characterization are given in SI Section  
 646 S11). Considering the single-component CO<sub>2</sub> adsorption  
 647 isotherms, a CO<sub>2</sub> “slip” (initial shock) of ~0.02 mol % was  
 648 predicted under dry flue gas at 40 °C (obtained from Golden’s  
 649 Rule, see Figure S54), corresponding to a capture rate of 99.5%  
 650 from a stream containing 4% CO<sub>2</sub> (calculated as (1–0.02/4) ×  
 651 100%). However, with dry simulated flue gas, approximately  
 652 0.6 mol % CO<sub>2</sub> slip was detected at the outlet, corresponding  
 653 to a lower maximum capture rate of 86%. In addition, the CO<sub>2</sub>  
 654 capacity at exhaustion (full breakthrough) was found to be 2.4  
 655 ± 0.2 mmol/g, which fell short of the capacity of 3.5 mmol/g  
 656 predicted from the adsorption isotherm. The breakthrough  
 657 profile and capacity were highly reproducible following  
 658 activation of the material at 120 °C under flowing He (Figure  
 659 S55). Reducing the flow rate to 14 sccm at 40 °C improved the  
 660 capture rate (~0.4 mol % slip, or 90% capture rate) and  
 661 sharpness of the breakthrough profile, reflecting a potential

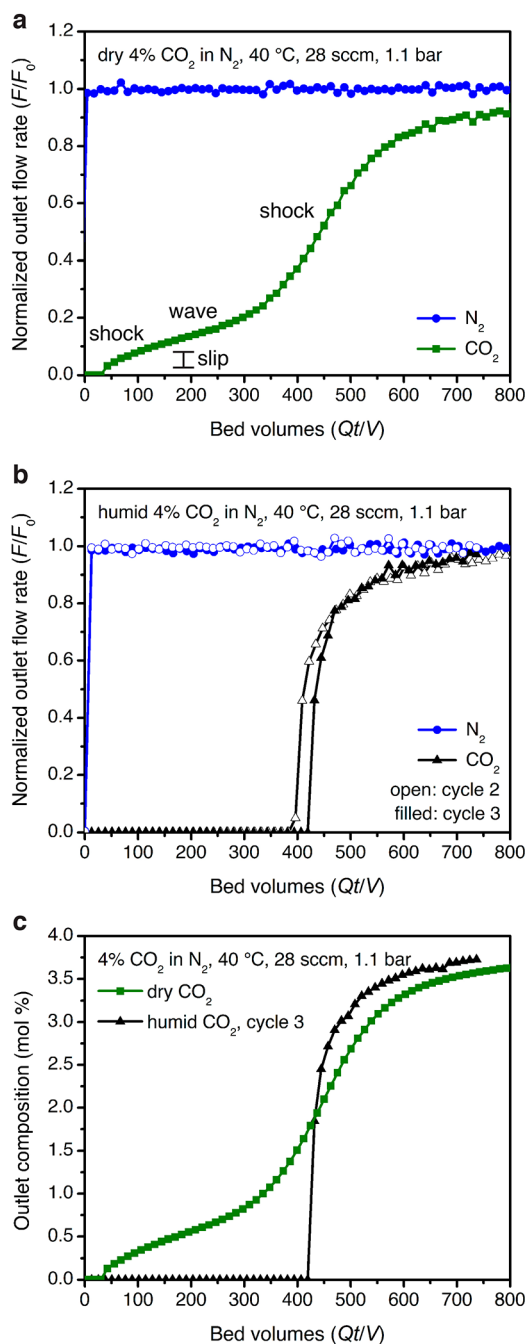


**Figure 4.** Breakthrough experiments with 2-ampd–Mg<sub>2</sub>(dobpdc) under 28 sccm of a simulated NGCC flue emission stream of 4% CO<sub>2</sub> in N<sub>2</sub> at 40 °C and ~1.1 bar. (a) Experiment with dry simulated flue gas. Capture rate: 86%; exhaustion capacity: 2.4 ± 0.2 mmol/g. (b) Second (filled symbols) and third (open symbols) breakthrough experiment cycles with humid flue gas following presaturation of the adsorbent bed with water. Capture rate: > 99%; usable capacity (average ≥90% capture): 2.2 and 2.3 ± 0.1 mmol/g; exhaustion capacity: 2.4 and 2.5 ± 0.1 mmol/g for 2nd and 3rd cycles, respectively. (c) Overlay of dry and humid (3<sup>rd</sup> cycle) CO<sub>2</sub> breakthrough profiles. The y-axis is shown as normalized outlet flow rate ( $F/F_0$ ) in (a) and (b) and as outlet composition in mol % in (c).

limitation in kinetics, but the breakthrough capacity at 662 exhaustion remained unchanged (Figure S56). As anticipated 663 from the isotherms and isobars, increasing the temperature to 664 60 °C increased the CO<sub>2</sub> slip, resulting in a measured capture 665 rate of only 62% (Figure S57; predicted capture rate, 88%). 666



667 The CO<sub>2</sub> breakthrough capacity at exhaustion was calculated  
668 as 2.2 ± 0.2 mmol/g, which again fell short of that predicted  
669 from the isotherm (3.2 mmol/g) but was consistent with that  
670 predicted from the CO<sub>2</sub> mixture isobars (2.2 mmol/g).  
671 Therefore, these results suggest that isobars collected by  
672 flowing dry CO<sub>2</sub> mixtures (Figure 3a) may reflect adsorbent  
673 performance in dry breakthrough measurements more  
674 accurately than single-component, volumetric isotherms  
675 (Figure 2). We anticipate that the greater utility of mixed-gas  
676 isobars versus single-component isotherms will apply generally  
677 in the evaluation of other carbon capture materials, particularly  
678 those with step-shaped adsorption isotherms.

679 To test the effect of CO<sub>2</sub> concentration on the elution  
680 profile, a breakthrough experiment was conducted under 14  
681 sccm of 15% CO<sub>2</sub> in N<sub>2</sub> at 40 °C and atmospheric pressure,  
682 simulating coal flue gas (Figure S58). In this experiment,  
683 negligible slip was observed (>99% CO<sub>2</sub> capture), and the CO<sub>2</sub>  
684 capacity (3.1 ± 0.2 mmol/g) was consistent with that of the  
685 equilibrium isotherm (3.6 mmol/g), considering the 92%  
686 diamine loading of the pellets. Therefore, the deviations from  
687 equilibrium behavior observed in breakthrough experiments  
688 with lower CO<sub>2</sub> concentrations (Figure 4), particularly with  
689 respect to high CO<sub>2</sub> slip and resulting low CO<sub>2</sub> capture rate,  
690 can likely be attributed to limitations in kinetics. As a result,  
691 nonequilibrium effects may limit the performance of diamine-  
692 appended frameworks with dry CO<sub>2</sub> mixtures at low partial  
693 pressures, a hypothesis supported by a recent investigation of  
694 another diamine-appended framework for CO<sub>2</sub> capture from  
695 air.<sup>84</sup>

696 We also evaluated the breakthrough behavior of the material  
697 under humid flue gas mixtures containing ~2 vol % H<sub>2</sub>O.  
698 Gratifyingly, consistent with the humid isobar measurements  
699 (Figure 3b), a dramatic enhancement in CO<sub>2</sub> capture  
700 performance was observed in breakthrough experiments with  
701 humid simulated NGCC flue gas following presaturation of the  
702 adsorbent bed with water (Figure 4b). In particular,  
703 humidification completely eliminated the initial CO<sub>2</sub> slip at  
704 40 °C, resulting in a CO<sub>2</sub> capture rate of >99% and a desirable  
705 single, sharp CO<sub>2</sub> breakthrough front. The CO<sub>2</sub> exhaustion  
706 capacity calculated at full breakthrough (2.4 ± 0.2 mmol/g)  
707 was equivalent to that of the dry experiment, with a usable  
708 CO<sub>2</sub> capacity of 2.2 ± 0.1 mmol/g satisfying the DoE target of  
709 an average of 90% CO<sub>2</sub> capture. This striking improvement in  
710 performance is clearly visible in an overlay of the dry and  
711 humid CO<sub>2</sub> breakthrough profiles at 40 °C (Figure 4c).  
712 Breakthrough experiments at 60 °C revealed similarly dramatic  
713 improvements in performance upon addition of humidity  
714 (Figures S59 and S60), with an increase in capture rate from  
715 62% to >99% (see Table S11 for a summary of capture rate  
716 results). The very high capture rate under humid conditions at  
717 60 °C suggests that even higher adsorption temperatures could  
718 be used to achieve smaller temperature swings. In ongoing  
719 work, we are developing methods to predict the breakthrough  
720 performance as a function of both relative humidity and  
721 temperature. The promising performance of 2-ampd-  
722 Mg<sub>2</sub>(dobpdc) in humid breakthrough experiments supports  
723 its utility as a next-generation adsorbent for postcombustion  
724 CO<sub>2</sub> capture from NGCC flue emissions.

725 **Influence of Water on CO<sub>2</sub> Adsorption.** Due to the  
726 sensitivity of the adsorption threshold to the local environment  
727 in cooperative adsorbents, it is of interest to determine whether  
728 the presence of water changes the nature of the chemisorbed  
729 phase or merely enhances the thermodynamic favorability of

the ammonium carbamate chain mechanism in diamine-  
appended metal-organic frameworks. Considering related  
materials, water is well-known to improve the CO<sub>2</sub> adsorption  
capacity of amine-functionalized silicas.<sup>30,42,88-99</sup> This effect is  
generally ascribed to a mechanistic shift from ammonium  
carbamate formation (0.5 CO<sub>2</sub>:amine) to bicarbonate or  
stabilized carbamic acid formation (1 CO<sub>2</sub> per  
amine),<sup>12,89-91,95,96,99-108</sup> although some studies have debated  
the formation of bicarbonates or carbonates.<sup>109-112</sup> Further-  
more, these reports largely focus on the influence of water on  
the adsorption capacity, with minimal discussion of the  
influence of water on the thermodynamics of adsorption and  
the desorption temperature.<sup>89,92,113,114</sup> Notably, our related  
vdW-corrected DFT study of the framework mmen-  
Mg<sub>2</sub>(dobpdc) demonstrated a stabilization of up to 41 kJ/  
mol for the CO<sub>2</sub>-inserted phase in the presence of water.<sup>115</sup>  
This result suggests that water enhances, rather than changes,  
the ammonium carbamate chain adsorption mechanism, but to  
date no study has yet combined experimental and computa-  
tional methods to characterize the effect of water on the CO<sub>2</sub>  
adsorption pathway, capacity, and breakthrough profile of a  
diamine-appended metal-organic framework. Accordingly, we  
employed IR and NMR spectroscopy and vdW-corrected DFT  
calculations to probe the behavior of 2-ampd-Mg<sub>2</sub>(dobpdc)  
under dry and humid conditions.

We first collected IR spectra of 2-ampd-Mg<sub>2</sub>(dobpdc) in  
the presence of dry N<sub>2</sub>, dry CO<sub>2</sub>, and humid CO<sub>2</sub> (Figure 5).  
756

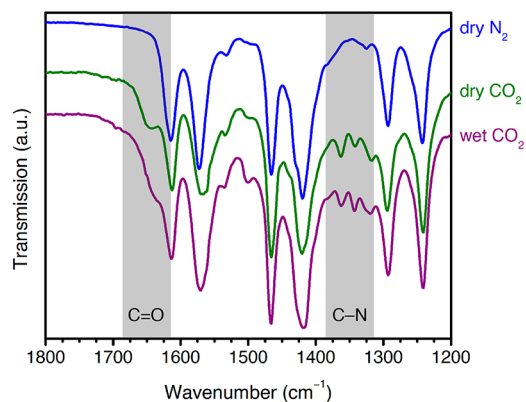


**Figure 5.** Infrared spectra of 2-ampd-Mg<sub>2</sub>(dobpdc) under dry N<sub>2</sub> (blue), dry CO<sub>2</sub> (green), and humid CO<sub>2</sub> (purple) at room temperature (~22 °C) and atmospheric pressure. The C(O)O<sup>-</sup> vibration at 1648 cm<sup>-1</sup> and C-N/N-C(O)O<sup>-</sup> vibrations at 1362 and 1342 cm<sup>-1</sup> are consistent with the proposed mechanism of ammonium carbamate chain formation under both dry and humid conditions.

Upon exposure to dry CO<sub>2</sub> at 22 °C and atmospheric pressure,  
broad C(O)O<sup>-</sup> (1648 cm<sup>-1</sup>) and sharp C-N/N-C(O)O<sup>-</sup>  
(1362 and 1342 cm<sup>-1</sup>) vibrations were observed, consistent  
with the anticipated ammonium carbamate chain mecha-  
nism.<sup>114</sup> Similar new vibrations were observed at 1637 and  
1340 cm<sup>-1</sup> in the IR spectrum of the molecular ammonium  
carbamate 2-ampd-CO<sub>2</sub> compared to the spectrum of free  
molecular 2-ampd (Figures S61-S63; crystallographic data  
provided as SI). We note that the reported C(O)O<sup>-</sup> stretches  
are shifted to higher energies compared to those generally  
assigned to carbamates in amine-functionalized silicas (1500-  
1600 cm<sup>-1</sup>),<sup>114</sup> which we attribute to the strong hydrogen  
bonding between the ammonium and carbamate units in these

770 materials. The presence of two C–N/N–C(O)O<sup>−</sup> stretches in  
 771 the IR spectrum of CO<sub>2</sub>-dosed 2-ampd–Mg<sub>2</sub>(dobpdc) further  
 772 suggests the formation of two distinct ammonium carbamate  
 773 products upon CO<sub>2</sub> adsorption. The C–N/N–C(O)O<sup>−</sup>  
 774 vibrations persist in the presence of humid CO<sub>2</sub>, consistent  
 775 with preservation of a chemisorptive mechanism, while the  
 776 C(O)O<sup>−</sup> band is obscured by the H–O–H bend at 1630 cm<sup>−1</sup>  
 777 arising from coadsorbed water.<sup>102</sup>

778 Solid-state NMR spectra obtained under dry and humid  
 779 conditions provided greater experimental detail for the effect of  
 780 water on CO<sub>2</sub> adsorption in 2-ampd–Mg<sub>2</sub>(dobpdc) (Figure  
 781 6). The <sup>13</sup>C NMR spectrum of 2-ampd–Mg<sub>2</sub>(dobpdc) dosed

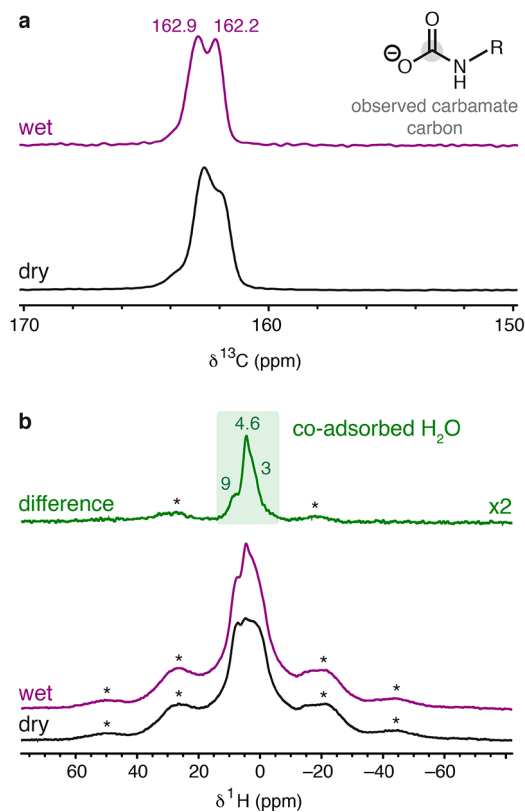


**Figure 6.** (a) <sup>13</sup>C NMR (16.4 T) MAS spectra of 2-ampd–Mg<sub>2</sub>(dobpdc) dosed with 1025 mbar of dry <sup>13</sup>CO<sub>2</sub> at 22 °C (bottom), and the same sample under a subsequent flow of humid, natural isotopic abundance CO<sub>2</sub> at atmospheric pressure (top). Spectra were obtained by cross-polarization from <sup>1</sup>H (contact time = 1 ms). Peaks corresponding to the framework linker are not observed due to the low natural abundance of <sup>13</sup>C nuclei in the framework compared to the 99% <sup>13</sup>C enrichment level for the chemisorbed CO<sub>2</sub>. (b) <sup>1</sup>H NMR spectra obtained by single-pulse excitation for the same samples as in (a). The MAS rate was 15 kHz in all cases. Asterisks mark spinning sidebands.

782 with 1025 mbar of <sup>13</sup>CO<sub>2</sub> at room temperature shows two  
 783 predominant overlapping resonances at 162 and 163 ppm, as  
 784 well as a weak shoulder at a higher chemical shift (Figure 6a),  
 785 all of which can be ascribed to chemisorbed CO<sub>2</sub> species. (See  
 786 Figure S87 for the <sup>13</sup>C spectrum of activated 2-ampd–  
 787 Mg<sub>2</sub>(dobpdc) prior to exposure to CO<sub>2</sub>.) We hypothesize that  
 788 the two main <sup>13</sup>C resonances (Figure 6a) correspond to two  
 789 conformations of ammonium carbamate chains,<sup>61</sup> consistent  
 790 with the IR spectrum collected under dry CO<sub>2</sub> (Figure 5).  
 791 Notably, our previous NMR characterization of diamines  
 792 exhibiting double-step CO<sub>2</sub> adsorption profiles also revealed

multiple resonances for chemisorbed CO<sub>2</sub>, which likely arise  
 due to spectroscopically distinct conformations of the sterically  
 hindered ammonium carbamate chains.<sup>61</sup> The weak shoulder  
 at higher frequencies (Figure 6a) may be associated with  
 incomplete equilibration (see Figure S90).

To interpret these results, we carried out additional 2D and  
<sup>15</sup>N NMR experiments. A <sup>1</sup>H–<sup>13</sup>C HETCOR experiment with  
 a short contact time (100 μs) was performed to probe  
 correlations with hydrogen atoms that are proximal to the  
 chemisorbed carbon species (i.e., within a few Å; Figure S89).  
 In the 2D experiment, the two <sup>13</sup>C resonances each show a  
 major <sup>1</sup>H correlation at ~5 ppm. We assign this feature to the  
 N–H group of an ammonium carbamate species, while the <sup>13</sup>C  
 peaks are attributed to the carbamate carbon atoms of two  
 distinct conformations of ammonium carbamate chains.<sup>61,116</sup>  
 The observed single N–H correlation supports CO<sub>2</sub> insertion  
 into metal–1° amine bonds to produce metal-bound  
 carbamate species, with proton transfer to neighboring  
 secondary amines to form charge-balancing ammonium  
 groups. This reactivity is consistent with the previous  
 crystallographic characterization of CO<sub>2</sub> insertion into  
 Zn<sub>2</sub>(dobpdc) functionalized with 1°/2° diamines.<sup>51</sup> Addition-  
 ally, the <sup>15</sup>N NMR spectrum of 2-ampd–Mg<sub>2</sub>(dobpdc) dosed  
 with 1025 mbar of <sup>13</sup>CO<sub>2</sub> featured two peaks at 46 and 76  
 ppm, consistent with nitrogen atoms in ammonium and  
 carbamate groups, respectively (Figure S86).<sup>50,61</sup>

After exposure of 2-ampd–Mg<sub>2</sub>(dobpdc) to a flow of humid  
 CO<sub>2</sub> (natural isotopic abundance) for 1 h, the main two <sup>13</sup>C  
 resonances were retained, but smaller line widths were  
 observed (Figure 6a; see also Figure S90 for similar data  
 obtained with a longer CO<sub>2</sub> exposure time). Therefore, in  
 further agreement with the IR data, these NMR spectra  
 demonstrate retention of the ammonium carbamate product in  
 the presence of water and exclude a water-induced change in  
 the CO<sub>2</sub> chemisorption mechanism. Co-adsorption of water  
 was also confirmed by collection of <sup>1</sup>H NMR spectra before  
 and after exposure to wet CO<sub>2</sub>. The difference <sup>1</sup>H spectrum  
 (Figure 6b) shows positive intensity that can be attributed to  
 coadsorbed water and reveals a narrow component at 4.6 ppm,  
 as well as broad components at ~9 and ~3 ppm. The highly  
 shifted (~9 ppm) water peak supports the formation of strong  
 hydrogen bonds following exposure to water (Figure 6b).  
 Additionally, the <sup>1</sup>H NMR spectra of 2-ampd–Mg<sub>2</sub>(dobpdc)  
 following exposure to dry or humid CO<sub>2</sub> (Figure 6b) show an  
 increase in line width of the amine resonances compared to the  
 NMR spectrum of activated 2-ampd–Mg<sub>2</sub>(dobpdc) (Figure  
 S88), consistent with a reduction of amine mobility following  
 CO<sub>2</sub> insertion.

Due to the structural complexity of 2-ampd–Mg<sub>2</sub>(dobpdc),  
 the CO<sub>2</sub>-inserted structure could not be solved directly from  
 the X-ray diffraction pattern of the microcrystalline powder or  
 from single crystals of the isostructural Zn framework under  
 dry or humid conditions. We thus turned to vdW-corrected  
 DFT calculations to predict the structure and energetics upon  
 CO<sub>2</sub> adsorption, H<sub>2</sub>O adsorption, and coadsorption of CO<sub>2</sub>  
 and H<sub>2</sub>O in 2-ampd–Mg<sub>2</sub>(dobpdc) (Figure 7). For simplicity,  
 all calculations were carried out using the left-handed  
 enantiomer of the diamine in the right-handed enantiomer of  
 the framework. An adsorption energy of −70 kJ/mol was  
 calculated for insertion of CO<sub>2</sub> to form ammonium carbamate  
 chains in Mg<sub>2</sub>(dobpdc)(2-ampd–CO<sub>2</sub>)<sub>2</sub>. This value is in good  
 agreement with the experimentally determined CO<sub>2</sub> adsorption  
 enthalpy of −72 ± 5 kJ/mol averaged over a loading of 0 to 1

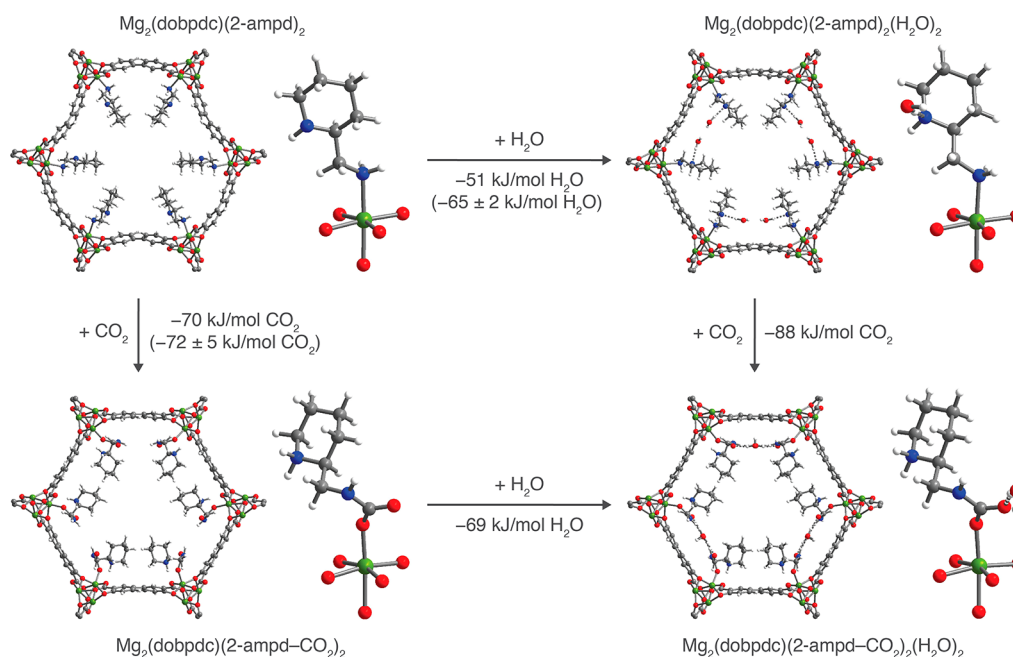


**Figure 7.** Projections along the pore axis and first coordination spheres of Mg(II) sites for the vdW-corrected, DFT-calculated structures of evacuated *L*-2-ampd-*R*-Mg<sub>2</sub>(dobpdc) (top left) and the framework following CO<sub>2</sub> insertion (bottom left), water adsorption (top right), and coadsorption of CO<sub>2</sub> and H<sub>2</sub>O (bottom right). The vdW-corrected, DFT-calculated binding energies ( $\Delta E$ ) are provided for each adsorption process, and available experimental differential binding enthalpies ( $\Delta h_{\text{ads}}$ ) are included in parentheses. Co-adsorption of water was found to enhance the CO<sub>2</sub> binding energy by  $-18$  kJ/mol, and a combined binding energy of  $-139$  kJ/mol 2-ampd was calculated for coadsorption of 1 CO<sub>2</sub> and 1 H<sub>2</sub>O per diamine. Green, blue, gray, red, and white spheres represent Mg, N, C, O, and H atoms, respectively.

856 CO<sub>2</sub> per diamine (Figure S8). In the calculated structure of  
 857 Mg<sub>2</sub>(dobpdc)(2-ampd)<sub>2</sub>(H<sub>2</sub>O)<sub>2</sub>, adsorbed water was found to  
 858 interact with 2-ampd by donating a hydrogen bond to the  
 859 secondary amine (O...N distance of 2.924 Å). Close H<sub>2</sub>O...  
 860 H<sub>2</sub>O contacts in the *ab* plane (O...O distance of 2.867 Å)  
 861 suggest that additional stabilization is provided by hydrogen  
 862 bonding between water molecules. In the absence of CO<sub>2</sub>, an  
 863 adsorption energy of  $-51$  kJ/mol was calculated for H<sub>2</sub>O. This  
 864 value is consistent with the experimental H<sub>2</sub>O adsorption  
 865 enthalpy of  $-50 \pm 2$  kJ/mol at low loadings (0.2 mmol/g, or  
 866 0.05 mmol H<sub>2</sub>O per diamine) but is slightly lower than the  
 867 average experimental enthalpy of  $-65 \pm 2$  kJ/mol over a  
 868 loading range of 0 to 1 mmol H<sub>2</sub>O per diamine (Figure S12).  
 869 In practice, while the structure shown here represents the  
 870 lowest-energy H<sub>2</sub>O binding mode discovered in our 0 K  
 871 calculations, H<sub>2</sub>O may sample other binding sites or  
 872 geometries within the pore at room temperature. Overall, the  
 873 adsorption energies corresponding to the calculated CO<sub>2</sub>- and  
 874 H<sub>2</sub>O-adsorbed structures of 2-ampd-Mg<sub>2</sub>(dobpdc) are in  
 875 reasonable agreement with those determined from single-  
 876 component adsorption measurements.

877 The DFT-calculated structure of Mg<sub>2</sub>(dobpdc)(2-ampd-  
 878 CO<sub>2</sub>)<sub>2</sub>(H<sub>2</sub>O)<sub>2</sub> shows a strong hydrogen bonding interaction  
 879 between H<sub>2</sub>O and the metal-bound oxygen atom of the  
 880 carbamate (O...O distance of 2.786 Å). Additionally, each  
 881 H<sub>2</sub>O molecule accepts a hydrogen bond from a carbamate  
 882 nitrogen atom of the neighboring ammonium carbamate chain  
 883 in the *ab* plane (N...O distance of 2.939 Å), resulting in a  
 884 channel of H<sub>2</sub>O molecules between adjacent ammonium  
 885 carbamate chains (Figure S95). A CO<sub>2</sub> adsorption energy of  
 886  $-88$  kJ/mol was calculated for coadsorption of 1 CO<sub>2</sub> and 1  
 887 H<sub>2</sub>O per diamine, indicating that water increases the  
 888 magnitude of the CO<sub>2</sub> binding energy by an estimated 18  
 889 kJ/mol compared to CO<sub>2</sub> insertion under dry conditions

(binding energy of  $-70$  kJ/mol). This value is smaller than the  
 890  $31 \pm 2$  kJ/mol increase in  $-\Delta h_{\text{ads}}$  calculated from the humid  
 891 vs dry pure CO<sub>2</sub> adsorption isobars, but a comparison of the  
 892 absolute values may be complicated by nonequilibrium effects  
 893 in the isobars and the inability to determine the precise  
 894 composition of the adsorbed phase. Notably, the DFT-  
 895 calculated binding energy of CO<sub>2</sub> is larger than that of water  
 896 in the coadsorbed structure, suggesting that the endothermic  
 897 penalty to desorb H<sub>2</sub>O is smaller, and thus H<sub>2</sub>O is likely to  
 898 desorb first. This result is consistent with the minimal  
 899 differences in the dry and humid CO<sub>2</sub> desorption temperatures  
 900 observed in mixed-gas isobars (Figure 3). We note that the  
 901 calculated and experimental NMR shifts for 2-ampd-  
 902 Mg<sub>2</sub>(dobpdc) exposed to dry and humid CO<sub>2</sub> also agree  
 903 well with the experimental values (Table S20).  
 904

Taken together, the humid isobars, breakthrough measure-  
 905 ments, spectroscopic data, and vdW-corrected DFT calcu-  
 906 lations support an increase in the favorability of CO<sub>2</sub> insertion  
 907 under humid conditions, as a result of an enhancement of the  
 908 ammonium carbamate chain formation mechanism in the  
 909 presence of water. In humid breakthrough experiments, the  
 910 resulting effective decrease in the isothermal CO<sub>2</sub> adsorption  
 911 step pressure alters the propagation of the adsorption front  
 912 through the bed. In particular, the single “shock” in the humid  
 913 CO<sub>2</sub> breakthrough profile suggests that water reduces the  
 914 effective step pressure and/or alters the shape of the CO<sub>2</sub>  
 915 adsorption profile at low partial pressures, leading to more  
 916 favorable performance under humid conditions (Figure S53).  
 917

**Thermal, Oxidative, and Cycling Stability.** Beyond the  
 918 thermodynamics and kinetics of adsorption, the long-term  
 919 stability of an adsorbent is a critical consideration for ultimate  
 920 industrial applications. In particular, the high oxygen content  
 921 of the NGCC flue gas stream ( $\sim 12\%$ ) is well-known to lead to  
 922 oxidative degradation of aqueous amine solutions.<sup>24–27</sup> To  
 923

924 evaluate the oxidative stability of 2-ampd-Mg<sub>2</sub>(dobpdc), the  
 925 material was exposed to a flow of dry air (~21% O<sub>2</sub> in N<sub>2</sub>) at  
 926 100 °C and atmospheric pressure for 5 h, and the dry, pure  
 927 CO<sub>2</sub> isobars were compared before and after exposure.  
 928 Minimal changes were observed in the CO<sub>2</sub> adsorption profile  
 929 or capacity after this extensive O<sub>2</sub> treatment (Figure 8). In

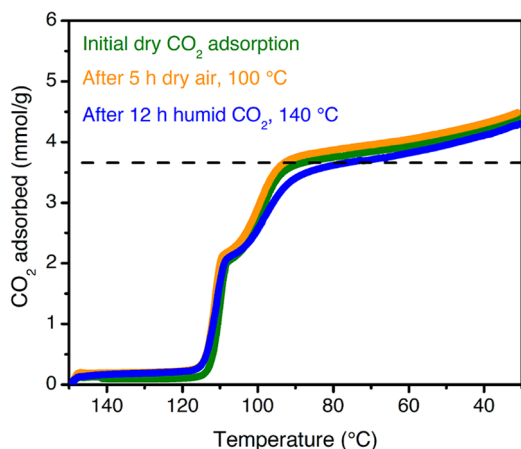


**Figure 8.** Dry, pure CO<sub>2</sub> adsorption isobars for 2-ampd-Mg<sub>2</sub>(dobpdc) as synthesized (green curve), after exposure to a flow of dry air (~21% O<sub>2</sub> in N<sub>2</sub>) at 100 °C for 5 h (orange curve), and after exposure to a flow of humid CO<sub>2</sub> at 140 °C for 12 h (blue curve). A ramp rate of 1 °C/min was used in all cases. The dashed black line indicates the theoretical capacity for adsorption of 1 CO<sub>2</sub> per diamine.

930 contrast, dry, oxygen-containing streams at 100 °C have been  
 931 found to cause significant degradation of silicas functionalized  
 932 with secondary amines.<sup>117</sup> In addition, no diamine oxidation  
 933 products were detected by IR or by <sup>1</sup>H NMR spectroscopy  
 934 after digestion of the O<sub>2</sub>-treated material (Figure S72). The  
 935 oxidative resistance of 2-ampd-Mg<sub>2</sub>(dobpdc) is likely due in  
 936 part to the fixed, wide spacing of diamines at metal sites ~7 Å  
 937 apart along the channel direction, which serves to mitigate  
 938 bimolecular (2 amine molecules) oxidation pathways observed  
 939 in other materials.<sup>117</sup>

940 Adsorbents for carbon capture from NGCC flue gas must  
 941 also withstand repeated thermal cycling under humid  
 942 conditions. As part of this work, we found that the stability  
 943 of diamine-appended variants of Mg<sub>2</sub>(dobpdc) and related  
 944 materials can be rapidly assessed by exposing the adsorbent to  
 945 a flow of humid CO<sub>2</sub> for 12 h at the relevant desorption  
 946 temperature (here, 140 °C) in a thermogravimetric analyzer,  
 947 simulating hundreds of adsorption/desorption cycles (SI  
 948 Section S16). The humid CO<sub>2</sub> adsorption capacities before  
 949 and after such accelerated decomposition experiments can be  
 950 compared to evaluate any capacity loss, and the material can be  
 951 digested after the test to detect diamine volatilization or  
 952 degradation. Notably, after treatment with flowing humid CO<sub>2</sub>  
 953 at 140 °C for 12 h, 2-ampd-Mg<sub>2</sub>(dobpdc) retains its step-  
 954 shaped adsorption profile (Figure 8, blue curve) with only a  
 955 slight capacity loss at 40 °C (original: 4.20 mmol/g; after  
 956 humid CO<sub>2</sub> treatment: 4.11 mmol/g). In addition, almost no  
 957 diamine volatilization (~2%) from the framework was  
 958 observed. We further tested the stability of 2-ampd-  
 959 Mg<sub>2</sub>(dobpdc) to accelerated decomposition experiments at  
 960 higher temperatures, representative of a potential process  
 961 failure. At temperatures as high as 180 °C, 2-ampd-

Mg<sub>2</sub>(dobpdc) retains more than 90% of its adsorption capacity 962  
 (Table S15), and the material remains highly crystalline even 963  
 after treatment with a humid CO<sub>2</sub> stream at 220 °C for 12 h 964  
 (Figure S70). Evaluation of a number of promising diamine- 965  
 appended variants of Mg<sub>2</sub>(dobpdc) for CO<sub>2</sub> capture from 966  
 NGCC flue gas further revealed that the thermal stability of 2- 967  
 ampd-Mg<sub>2</sub>(dobpdc) is nearly unparalleled among this family 968  
 of materials (Table S14). In addition, the stability of 2-ampd- 969  
 Mg<sub>2</sub>(dobpdc) is far superior to that of the representative 970  
 amine-functionalized silica MCM-41-PEI-50, which undergoes 971  
 urea formation and significant capacity loss (~17%) at 40 °C 972  
 following exposure to humid CO<sub>2</sub> for 12 h at 140 °C (Figures 973  
 S75–S77). The exceptional stability of 2-ampd-Mg<sub>2</sub>(dobpdc) 974  
 to humid gas streams at high temperatures makes it particularly 975  
 promising for long-term application in a CO<sub>2</sub> capture process. 976

The stability of 2-ampd-Mg<sub>2</sub>(dobpdc) in a TSA process 977  
 was further evaluated by performing 750 adsorption (humid 978  
 4% CO<sub>2</sub> in N<sub>2</sub>, 40 °C) and desorption (humid CO<sub>2</sub>, 140 °C) 979  
 cycles using a thermogravimetric analyzer (Figure 9, see SI 980-99

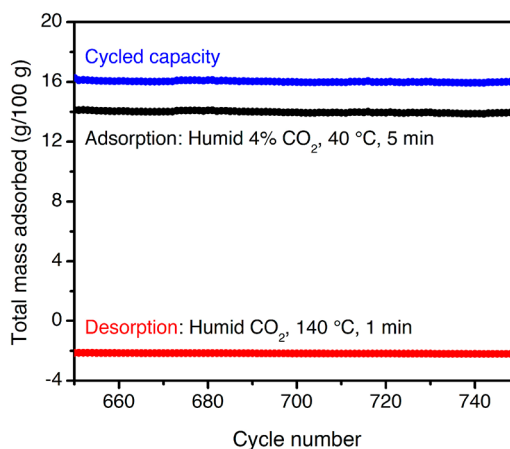


**Figure 9.** Cycling data for the final 100 of 750 adsorption/desorption cycles for 2-ampd-Mg<sub>2</sub>(dobpdc) in a simulated temperature swing adsorption process. Adsorption: humid 4% CO<sub>2</sub> in N<sub>2</sub>, 40 °C, 5 min (black, cycle maxima). Desorption: Humid CO<sub>2</sub>, 140 °C, 1 min (red, cycle minima). The cycled capacity (difference) is shown in blue. The baseline value of 0 g/100 g is defined as the mass after activation under 4% CO<sub>2</sub> in N<sub>2</sub> at 150 °C for 20 min prior to the first cycle. The diamine loading was reduced from 100% to 94% after this experiment. The same final loading was observed after 200 adsorption/desorption cycles, suggesting that the diamine loading stabilizes after initial loss. The weight loss due to diamine volatilization correlates with equilibration of the mass upon desorption to the observed negative baseline value.

Figure S80 for the full cycling data). Consistent with the 981  
 accelerated decomposition test results (Figure 8), 2-ampd- 982  
 Mg<sub>2</sub>(dobpdc) exhibited a stable cycling capacity under humid 983  
 simulated NGCC flue gas (Figure 9). The same final diamine 984  
 loading (~94%) was observed after both 200 and 750 cycles, 985  
 suggesting that the loading stabilizes after a small amount of 986  
 initial diamine volatilization, likely from weakly bound defect 987  
 or surface sites. Notably, a high CO<sub>2</sub>/H<sub>2</sub>O cycling capacity of 988  
 16.0 g/100 g was observed for the 750<sup>th</sup> cycle, comparable to 989  
 the adsorption capacity from a dry 4% CO<sub>2</sub> in N<sub>2</sub> stream at 40 990  
 °C (15.8 g/100 g). Nearly the same cycled capacity (15.3 g/ 991  
 100 g) could also be achieved over 200 tested cycles with a 992  
 higher adsorption temperature of 60 °C (Figure S81). Short 993  
 adsorption (5 min) and desorption (1 min) times were used in 994

995 these experiments, indicating rapid kinetics despite the low  
996 CO<sub>2</sub> content of the simulated flue gas stream. Overall, the  
997 exceptional stability of 2-ampd–Mg<sub>2</sub>(dobpdc) and excellent  
998 performance in breakthrough and cycling experiments support  
999 further development of this promising adsorbent for CO<sub>2</sub>  
1000 capture from the emissions of gas-fired power plants.

## 1001 ■ CONCLUSIONS

1002 Natural gas offers significant environmental advantages as an  
1003 alternative to coal by enabling approximately 50% lower CO<sub>2</sub>  
1004 emissions per unit of electricity produced. Capturing and  
1005 sequestering the CO<sub>2</sub> emissions from gas-fired power plants  
1006 provides an attractive option to achieve even greater emission  
1007 reductions. We have shown that the metal–organic framework  
1008 2-ampd–Mg<sub>2</sub>(dobpdc) is a promising candidate for post-  
1009 combustion CO<sub>2</sub> capture from the emissions of NGCC power  
1010 stations. In particular, as a result of the constituent cyclic  
1011 diamine, this material overcomes the trade-off between stability  
1012 and capacity encountered with related cooperative adsorbents  
1013 featuring linear 1°/2° diamines. Importantly, in breakthrough  
1014 experiments simulating a fixed-bed adsorption process, 2-  
1015 ampd–Mg<sub>2</sub>(dobpdc) exhibits single-shock breakthrough pro-  
1016 files under humid conditions, in contrast to the multimodal  
1017 elution profiles observed under dry conditions. This advanta-  
1018 geous result is attributed to stabilizing H<sub>2</sub>O–carbamate  
1019 interactions, a conclusion supported by mixed-gas adsorption  
1020 experiments, spectroscopic characterization, and vdW-cor-  
1021 rected DFT calculations. Finally, 2-ampd–Mg<sub>2</sub>(dobpdc)  
1022 achieves the challenging practical criteria required of a material  
1023 for CCS from NGCC emissions, namely a high CO<sub>2</sub> swing  
1024 capacity as well as high thermal, oxidative, and cycling stability.  
1025 Continued development of 2-ampd–Mg<sub>2</sub>(dobpdc) at larger  
1026 scales and in structured forms will enable modeling of heat and  
1027 mass transfer and support bench-scale testing.

1028 More broadly, this report achieves key advances toward the  
1029 deployment of cooperative adsorbents in industrial CO<sub>2</sub>  
1030 separations. First, we have reiterated the importance of  
1031 considering CO<sub>2</sub> “slip” in adsorbent and process design for  
1032 CO<sub>2</sub> capture applications with dry mixtures.<sup>45,84</sup> Second, and  
1033 most importantly, we have established that presaturating the  
1034 adsorbent bed with water can significantly enhance the CO<sub>2</sub>  
1035 capture performance of diamine-appended, cooperative  
1036 adsorbents by mitigating or eliminating CO<sub>2</sub> slip. Third, we  
1037 have shown that experiments under flow conditions (such as  
1038 isobars collected with slow temperature ramp rates under  
1039 varying CO<sub>2</sub> concentrations) may predict the performance of  
1040 cooperative adsorbents more accurately than single-compo-  
1041 nent, volumetric adsorption isotherms. Finally, we have shown  
1042 that TSA processes with cooperative adsorbents can utilize  
1043 higher adsorption temperatures (here, 60 °C or higher instead  
1044 of 40 °C) that could serve to mitigate water coadsorption and  
1045 reduce operating costs related to cooling the flue gas stream.  
1046 Moving forward, we expect that these discoveries will be of  
1047 value in the design of cooperative adsorbents for other  
1048 challenging CO<sub>2</sub> capture processes, such as the direct capture  
1049 of CO<sub>2</sub> from air.

Full characterization of all adsorbents and additional 1054  
experimental details (PDF) 1055  
Crystallographic data for Zn<sub>2</sub>(dobpdc)(2- 1056  
ampd)<sub>1.76</sub>(C<sub>7</sub>H<sub>8</sub>)<sub>0.79</sub> (CIF) 1057  
Crystallographic data for 2-ampd–CO<sub>2</sub> (CIF) 1058  
DFT-calculated structure of Mg<sub>2</sub>(dobpdc)(2-ampd)<sub>2</sub> 1059  
(CIF) 1060  
DFT-calculated structure of Mg<sub>2</sub>(dobpdc)(2-ampd– 1061  
CO<sub>2</sub>)<sub>2</sub> (CIF) 1062  
DFT-calculated structure of Mg<sub>2</sub>(dobpdc)(2- 1063  
ampd)<sub>2</sub>(H<sub>2</sub>O)<sub>2</sub> (CIF) 1064  
DFT-calculated structure of Mg<sub>2</sub>(dobpdc)(2-ampd– 1065  
CO<sub>2</sub>)<sub>2</sub>(H<sub>2</sub>O)<sub>2</sub> (CIF) 1066  
DFT-calculated structure of cocaine (CIF) 1067  
DFT-calculated structure of glycine (CIF) 1068

## 1069 ■ AUTHOR INFORMATION

### 1070 Corresponding Author

1071 \*jrlong@berkeley.edu

### 1072 ORCID

1073 Phillip J. Milner: 0000-0002-2618-013X

1074 Alexander C. Forse: 0000-0001-9592-9821

1075 Jeffrey A. Reimer: 0000-0002-4191-3725

1076 Simon C. Weston: 0000-0002-7439-5055

1077 Jeffrey R. Long: 0000-0002-5324-1321

### 1078 Present Address

1079 ♦Department of Chemistry and Chemical Biology, Cornell  
1080 University, Ithaca, New York, 14853, United States.

### 1081 Author Contributions

1082 ¶These authors contributed equally to this work.

### 1083 Notes

1084 The authors declare the following competing financial  
1085 interest(s): J.R.L. has a financial interest in Mosaic Materials,  
1086 Inc., a start-up company working to commercialize metal-  
1087 organic frameworks for gas separations. The University of  
1088 California, Berkeley and ExxonMobil Research and Engineer-  
1089 ing Company have applied for a patent on some of the  
1090 materials discussed herein, on which P.J.M., R.L.S., S.C.W., and  
1091 J.R.L. are included as inventors.

## 1092 ■ ACKNOWLEDGMENTS

1093 We gratefully acknowledge ExxonMobil Research and  
1094 Engineering Company for financial support of this work. We  
1095 thank the National Institute of General Medical Sciences of the  
1096 National Institutes of Health for a postdoctoral fellowship for  
1097 P.J.M. (F32GM120799). The content is solely the responsi-  
1098 bility of the authors and does not necessarily represent the  
1099 official views of the National Institutes of Health. We thank the  
1100 Philomathia Foundation and Berkeley Energy and Climate  
1101 Institute for support of A.C.F. through a postdoctoral  
1102 fellowship. Work at the Molecular Foundry was supported  
1103 by the Office of Science, Office of Basic Energy Sciences, U.S.  
1104 Department of Energy, under Contract DE-AC02-  
1105 05CH11231, and computational resources were provided by  
1106 the Department of Energy (LBNL Lawrence Livermore and NERSC).  
1107 This research also used the Savio computational cluster  
1108 resource provided by the Berkeley Research Computing  
1109 program at the University of California, Berkeley (supported  
1110 by the UC Berkeley Chancellor, Vice Chancellor for Research,  
1111 and Chief Information Officer). Single-crystal X-ray diffraction  
1112 data were collected on Beamline 12.2.1 at the Advanced Light

1113 Source at Lawrence Berkeley National Laboratory, which is  
1114 supported by the Director, Office of Science, Office of Basic  
1115 Energy Sciences, of the U.S. Department of Energy under  
1116 Contract No. DE-AC02-05CH11231. Synchrotron powder X-  
1117 ray diffraction data were collected at the Advanced Photon  
1118 Source, a U.S. Department of Energy Office of Science User  
1119 Facility operated for the DOE Office of Science by Argonne  
1120 National Laboratory under Contract No. DE-AC02-  
1121 06CH11357. We thank Dr. Joseph Falkowski (ExxonMobil  
1122 Research and Engineering Company), Dr. Miguel Gonzalez  
1123 (UC Berkeley), and Dr. Jeffrey Martell (UC Berkeley) for  
1124 helpful discussions; Eugene Kim (UC Berkeley) and Julia  
1125 Oktawiec (UC Berkeley) for experimental assistance; and Dr.  
1126 Katie Meihaus (UC Berkeley) for editorial assistance.

## 1127 ■ REFERENCES

- 1128 (1) *CO<sub>2</sub> Emissions from Fuel Combustion 2017—Highlights*; Interna-  
1129 tional Energy Agency: Paris, France, 2017.
- 1130 (2) Pachauri, R. K.; Allen, M. R.; Barros, V. R.; Broome, J.; Cramer,  
1131 W.; Christ, R.; Church, J. A.; Clarke, L.; Dahe, Q.; Dasgupta, P.  
1132 *Climate Change 2014: Synthesis Report. Contribution of Working Groups*  
1133 *I, II and III to the Fifth Assessment Report of the Intergovernmental Panel*  
1134 *on Climate Change*; IPCC, 2014.
- 1135 (3) Chu, S. Carbon Capture and Sequestration. *Science* **2009**, *325*  
1136 (5948), 1599–1599.
- 1137 (4) Bui, M.; Adjiman, C. S.; Bardow, A.; Anthony, E. J.; Boston, A.;  
1138 Brown, S.; Fennell, P. S.; Fuss, S.; Galindo, A.; Hackett, L. A.; Hallett,  
1139 J. P.; Herzog, H. J.; Jackson, G.; Kemper, J.; Krevor, S.; Maitland, G.  
1140 C.; Matuszewski, M.; Metcalfe, I. S.; Petit, C.; Puxty, G.; Reimer, J.;  
1141 Reiner, D. M.; Rubin, E. S.; Scott, S. A.; Shah, N.; Smit, B.; Trusler, J.  
1142 P. M.; Webley, P.; Wilcox, J.; Mac Dowell, N. Carbon Capture and  
1143 Storage (CCS): The Way Forward. *Energy Environ. Sci.* **2018**, *11*,  
1144 1062–1076.
- 1145 (5) Stauffer, P. H.; Keating, G. N.; Middleton, R. S.; Viswanathan,  
1146 H. S.; Berchtold, K. A.; Singh, R. P.; Pawar, R. J.; Mancino, A.  
1147 Greening Coal: Breakthroughs and Challenges in Carbon Capture  
1148 and Storage. *Environ. Sci. Technol.* **2011**, *45* (20), 8597–8604.
- 1149 (6) *World Energy Outlook 2017*; International Energy Agency, 2017.  
1150 DOI: 10.1787/weo-2017-en.
- 1151 (7) *Annual Energy Outlook 2018 with Projections to 2050*; U.S.  
1152 Energy Information Administration, 2018.
- 1153 (8) *CO<sub>2</sub> Capture at Gas Fired Power Plants*; IEAGHG, 2012.
- 1154 (9) *Carbon Dioxide Capture for Natural Gas and Industrial*  
1155 *Applications; Quadrennial Technology Review 2015*; U.S. Department  
1156 of Energy, 2015.
- 1157 (10) *Carbon Capture Opportunities for Natural Gas Fired Power*  
1158 *Systems*; U.S. Department of Energy, 2017.
- 1159 (11) *Cost and Performance Baseline for Fossil Energy Plants. Vol. 1a:*  
1160 *Bituminous Coal (PC) and Natural Gas to Electricity, Revision 3*;  
1161 DOE/NETL-2015/1723; U.S. Department of Energy, National  
1162 Energy Technology Laboratory, 2015.
- 1163 (12) Khatri, R. A.; Chuang, S. S. C.; Soong, Y.; Gray, M. Thermal  
1164 and Chemical Stability of Regenerable Solid Amine Sorbent for CO<sub>2</sub>  
1165 Capture. *Energy Fuels* **2006**, *20* (4), 1514–1520.
- 1166 (13) Uyanga, I. J.; Idem, R. O. Studies of SO<sub>2</sub>- and O<sub>2</sub>-Induced  
1167 Degradation of Aqueous MEA during CO<sub>2</sub> Capture from Power Plant  
1168 Flue Gas Streams. *Ind. Eng. Chem. Res.* **2007**, *46* (8), 2558–2566.
- 1169 (14) Belmabkhout, Y.; Sayari, A. Isothermal versus Non-Isothermal  
1170 Adsorption-Desorption Cycling of Triamine-Grafted Pore-Expanded  
1171 MCM-41 Mesoporous Silica for CO<sub>2</sub> Capture from Flue Gas. *Energy*  
1172 *Fuels* **2010**, *24* (9), 5273–5280.
- 1173 (15) Sjostrom, S.; Krutka, H. Evaluation of Solid Sorbents as a  
1174 Retrofit Technology for CO<sub>2</sub> Capture. *Fuel* **2010**, *89* (6), 1298–1306.
- 1175 (16) Han, S.; Huang, Y.; Watanabe, T.; Dai, Y.; Walton, K. S.; Nair,  
1176 S.; Sholl, D. S.; Meredith, J. C. High-Throughput Screening of Metal-  
1177 Organic Frameworks for CO<sub>2</sub> Separation. *ACS Comb. Sci.* **2012**, *14*  
1178 (4), 263–267.
- (17) Yu, K.; Kiesling, K.; Schmidt, J. R. Trace Flue Gas  
Contaminants Poison Coordinatively Unsaturated Metal–Organic  
Frameworks: Implications for CO<sub>2</sub> Adsorption and Separation. *J.*  
*Phys. Chem. C* **2012**, *116* (38), 20480–20488.
- (18) Hallenbeck, A. P.; Kitchin, J. R. Effects of O<sub>2</sub> and SO<sub>2</sub> on the  
Capture Capacity of a Primary-Amine Based Polymeric CO<sub>2</sub> Sorbent.  
*Ind. Eng. Chem. Res.* **2013**, *52* (31), 10788–10794.
- (19) Rezaei, F.; Jones, C. W. Stability of Supported Amine  
Adsorbents to SO<sub>2</sub> and NO<sub>x</sub> in Postcombustion CO<sub>2</sub> Capture. 1.  
Single-Component Adsorption. *Ind. Eng. Chem. Res.* **2013**, *52* (34),  
12192–12201.
- (20) Berger, A. H.; Bhowan, A. S. Selection of Optimal Solid Sorbents  
for CO<sub>2</sub> Capture Based on Gas Phase CO<sub>2</sub> Composition. *Energy*  
*Procedia* **2014**, *63*, 2092–2099.
- (21) Rezaei, F.; Grahn, M. Thermal Management of Structured  
Adsorbents in CO<sub>2</sub> Capture Processes. *Ind. Eng. Chem. Res.* **2012**, *51*  
(10), 4025–4034.
- (22) Rochelle, G. T. Amine Scrubbing for CO<sub>2</sub> Capture. *Science*  
**2009**, *325* (5948), 1652–1654.
- (23) Bhowan, A. S.; Freeman, B. C. Analysis and Status of Post-  
Combustion Carbon Dioxide Capture Technologies. *Environ. Sci.*  
*Technol.* **2011**, *45* (20), 8624–8632.
- (24) Gouedard, C.; Picq, D.; Launay, F.; Carrette, P.-L. Amine  
Degradation in CO<sub>2</sub> Capture. I. A Review. *Int. J. Greenhouse Gas*  
*Control* **2012**, *10*, 244–270.
- (25) Fredriksen, S. B.; Jens, K.-J. Oxidative Degradation of Aqueous  
Amine Solutions of MEA, AMP, MDEA, Pz: A Review. *Energy*  
*Procedia* **2013**, *37*, 1770–1777.
- (26) Vega, F.; Sanna, A.; Navarrete, B.; Maroto-Valer, M. M.;  
Cortés, V. J. Degradation of Amine-based Solvents in CO<sub>2</sub> Capture  
Process by Chemical Absorption. *Greenhouse Gases: Sci. Technol.*  
**2014**, *4* (6), 707–733.
- (27) Mazari, S. A.; Si Ali, B.; Jan, B. M.; Saeed, I. M.; Nizamuddin, S.  
An Overview of Solvent Management and Emissions of Amine-Based  
CO<sub>2</sub> Capture Technology. *Int. J. Greenhouse Gas Control* **2015**, *34*,  
129–140.
- (28) Choi, S.; Drese, J. H.; Jones, C. W. Adsorbent Materials for  
Carbon Dioxide Capture from Large Anthropogenic Point Sources.  
*ChemSusChem* **2009**, *2* (9), 796–854.
- (29) Bae, Y.-S.; Snurr, R. Q. Development and Evaluation of Porous  
Materials for Carbon Dioxide Separation and Capture. *Angew. Chem.,*  
*Int. Ed.* **2011**, *50* (49), 11586–11596.
- (30) Bollini, P.; Didas, S. A.; Jones, C. W. Amine-Oxide Hybrid  
Materials for Acid Gas Separations. *J. Mater. Chem.* **2011**, *21* (39),  
15100–15120.
- (31) Li, J.-R.; Ma, Y.; McCarthy, M. C.; Sculley, J.; Yu, J.; Jeong, H.-  
K.; Balbuena, P. B.; Zhou, H.-C. Carbon Dioxide Capture-Related  
Gas Adsorption and Separation in Metal-Organic Frameworks. *Coord.*  
*Chem. Rev.* **2011**, *255* (15–16), 1791–1823.
- (32) Wang, Q.; Luo, J.; Zhong, Z.; Borgna, A. CO<sub>2</sub> Capture by Solid  
Adsorbents and Their Applications: Current Status and New Trends.  
*Energy Environ. Sci.* **2011**, *4* (1), 42–55.
- (33) Liu, J.; Thallapally, P. K.; McGrail, B. P.; Brown, D. R.; Liu, J.  
Progress in Adsorption-Based CO<sub>2</sub> Capture by Metal–Organic  
Frameworks. *Chem. Soc. Rev.* **2012**, *41* (6), 2308–2322.
- (34) Samanta, A.; Zhao, A.; Shimizu, G. K. H.; Sarkar, P.; Gupta, R.  
Post-Combustion CO<sub>2</sub> Capture Using Solid Sorbents: A Review. *Ind.*  
*Eng. Chem. Res.* **2012**, *51* (4), 1438–1463.
- (35) Sumida, K.; Rogow, D. L.; Mason, J. A.; McDonald, T. M.;  
Bloch, E. D.; Herm, Z. R.; Bae, T.-H.; Long, J. R. Carbon Dioxide  
Capture in Metal–Organic Frameworks. *Chem. Rev.* **2012**, *112* (2),  
724–781.
- (36) Huck, J. M.; Lin, L.-C.; Berger, A. H.; Shahrak, M. N.; Martin,  
R. L.; Bhowan, A. S.; Haranczyk, M.; Reuter, K.; Smit, B. Evaluating  
Different Classes of Porous Materials for Carbon Capture. *Energy*  
*Environ. Sci.* **2014**, *7* (12), 4132–4146.
- (37) Webley, P. A. Adsorption Technology for CO<sub>2</sub> Separation and  
Capture: A Perspective. *Adsorption* **2014**, *20* (2–3), 225–231.

- 1247 (38) Lee, S.-Y.; Park, S.-J. A Review on Solid Adsorbents for Carbon  
1248 Dioxide Capture. *J. Ind. Eng. Chem.* **2015**, *23*, 1–11.
- 1249 (39) Sanz-Pérez, E. S.; Murdock, C. R.; Didas, S. A.; Jones, C. W.  
1250 Direct Capture of CO<sub>2</sub> from Ambient Air. *Chem. Rev.* **2016**, *116* (19),  
1251 11840–11876.
- 1252 (40) Unveren, E. E.; Monkul, B. O.; Sartoglan, S.; Karademir, N.;  
1253 Alper, E. Solid Amine Sorbents for CO<sub>2</sub> Capture by Chemical  
1254 Adsorption: A Review. *Petroleum* **2017**, *3* (1), 37–50.
- 1255 (41) Siegelman, R. L.; Milner, P. J.; Kim, E. J.; Weston, S. C.; Long,  
1256 J. R. Challenges and Opportunities for Adsorption-Based CO<sub>2</sub>  
1257 Capture from Natural Gas Combined Cycle Emissions. *Energy*  
1258 *Environ. Sci.* **2019**, *12* (7), 2161–2173.
- 1259 (42) Xu, X.; Song, C.; Miller, B. G.; Scaroni, A. W. Adsorption  
1260 Separation of Carbon Dioxide from Flue Gas of Natural Gas-Fired  
1261 Boiler by a Novel Nanoporous “Molecular Basket” Adsorbent. *Fuel*  
1262 *Process. Technol.* **2005**, *86* (14), 1457–1472.
- 1263 (43) Grande, C. A.; Ribeiro, R. P. P. L.; Rodrigues, A. E. CO<sub>2</sub>  
1264 Capture from NGCC Power Stations Using Electric Swing  
1265 Adsorption (ESA). *Energy Fuels* **2009**, *23* (5), 2797–2803.
- 1266 (44) Seif El Nasr, A.; Nelson, T.; Kataria, A.; Abu-Zahra, M. R. M.  
1267 Benchmarking of a Novel Solid Sorbent CO<sub>2</sub> Capture Process for  
1268 NGCC Power Generation. *Int. J. Greenhouse Gas Control* **2015**, *42*,  
1269 583–592.
- 1270 (45) Hefti, M.; Joss, L.; Bjelobrk, Z.; Mazzotti, M. On the Potential  
1271 of Phase-Change Adsorbents for CO<sub>2</sub> Capture by Temperature Swing  
1272 Adsorption. *Faraday Discuss.* **2016**, *192*, 153–179.
- 1273 (46) Gibson, J. A. A.; Mangano, E.; Shiko, E.; Greenaway, A. G.;  
1274 Gromov, A. V.; Lozinska, M. M.; Friedrich, D.; Campbell, E. E. B.;  
1275 Wright, P. A.; Brandani, S. Adsorption Materials and Processes for  
1276 Carbon Capture from Gas-Fired Power Plants: AMPGas. *Ind. Eng.*  
1277 *Chem. Res.* **2016**, *55* (13), 3840–3851.
- 1278 (47) Zhang, W.; Sun, C.; Snape, C. E.; Irons, R.; Stebbing, S.;  
1279 Alderson, T.; Fitzgerald, D.; Liu, H. Process Simulations of Post-  
1280 Combustion CO<sub>2</sub> Capture for Coal and Natural Gas-Fired Power  
1281 Plants Using a Polyethyleneimine/Silica Adsorbent. *Int. J. Greenhouse*  
1282 *Gas Control* **2017**, *58*, 276–289.
- 1283 (48) Dijkstra, J. W.; Walspurger, S.; Elzinga, G. D.; Pieterse, J. A. Z.;  
1284 Boon, J.; Haije, W. G. Evaluation of Postcombustion CO<sub>2</sub> Capture by  
1285 a Solid Sorbent with Process Modeling Using Experimental CO<sub>2</sub> and  
1286 H<sub>2</sub>O Adsorption Characteristics. *Ind. Eng. Chem. Res.* **2018**, *57* (4),  
1287 1245–1261.
- 1288 (49) McDonald, T. M.; Lee, W. R.; Mason, J. A.; Wiers, B. M.;  
1289 Hong, C. S.; Long, J. R. Capture of Carbon Dioxide from Air and Flue  
1290 Gas in the Alkylamine-Appended Metal–Organic Framework mmen-  
1291 Mg<sub>2</sub>(dobpdc). *J. Am. Chem. Soc.* **2012**, *134* (16), 7056–7065.
- 1292 (50) McDonald, T. M.; Mason, J. A.; Kong, X.; Bloch, E. D.; Gygi,  
1293 D.; Dani, A.; Crocellà, V.; Giordanino, F.; Odoh, S. O.; Drisdell, W.  
1294 S.; Vlasisavljevich, B.; Dzubak, A. L.; Poloni, R.; Schnell, S. K.; Planas,  
1295 N.; Lee, K.; Pascal, T.; Wan, L. F.; Prendergast, D.; Neaton, J. B.;  
1296 Smit, B.; Kortright, J. B.; Gagliardi, L.; Bordiga, S.; Reimer, J. A.;  
1297 Long, J. R. Cooperative Insertion of CO<sub>2</sub> in Diamine-Appended  
1298 Metal–Organic Frameworks. *Nature* **2015**, *519* (7543), 303–308.
- 1299 (51) Siegelman, R. L.; McDonald, T. M.; Gonzalez, M. I.; Martell, J.  
1300 D.; Milner, P. J.; Mason, J. A.; Berger, A. H.; Bhowan, A. S.; Long, J. R.  
1301 Controlling Cooperative CO<sub>2</sub> Adsorption in Diamine-Appended  
1302 Mg<sub>2</sub>(dobpdc) Metal–Organic Frameworks. *J. Am. Chem. Soc.* **2017**,  
1303 *139* (30), 10526–10538.
- 1304 (52) Milner, P. J.; Siegelman, R. L.; Forse, A. C.; Gonzalez, M. I.;  
1305 Runčevski, T.; Martell, J. D.; Reimer, J. A.; Long, J. R. A  
1306 Diaminopropane-Appended Metal–Organic Framework Enabling  
1307 Efficient CO<sub>2</sub> Capture from Coal Flue Gas via a Mixed Adsorption  
1308 Mechanism. *J. Am. Chem. Soc.* **2017**, *139* (38), 13541–13553.
- 1309 (53) Milner, P. J.; Martell, J. D.; Siegelman, R. L.; Gygi, D.; Weston,  
1310 S. C.; Long, J. R. Overcoming Double-Step CO<sub>2</sub> Adsorption and  
1311 Minimizing Water Co-Adsorption in Bulky Diamine-Appended  
1312 Variants of Mg<sub>2</sub>(dobpdc). *Chem. Sci.* **2018**, *9* (1), 160–174.
- 1313 (54) Lee, W. R.; Hwang, S. Y.; Ryu, D. W.; Lim, K. S.; Han, S. S.;  
1314 Moon, D.; Choi, J.; Hong, C. S. Diamine-Functionalized Metal–  
1315 Organic Framework: Exceptionally High CO<sub>2</sub> Capacities for  
Ambient Air and Flue Gas, Ultrafast CO<sub>2</sub> Uptake Rate, and  
Adsorption Mechanism. *Energy Environ. Sci.* **2014**, *7* (2), 744–751.
- (55) Lee, W. R.; Jo, H.; Yang, L.-M.; Lee, H.; Ryu, D. W.; Lim, K. S.;  
Song, J. H.; Min, D. Y.; Han, S. S.; Seo, J. G.; Park, Y. K.; Moon, D.;  
Hong, C. S. Exceptional CO<sub>2</sub> Working Capacity in a Heterodiamine-  
Grafted Metal–Organic Framework. *Chem. Sci.* **2015**, *6* (7), 3697–  
3705.
- (56) Jo, H.; Lee, W. R.; Kim, N. W.; Jung, H.; Lim, K. S.; Kim, J. E.;  
Kang, D. W.; Lee, H.; Hiremath, V.; Seo, J. G.; Jin, H.; Moon, D.;  
Han, S. S.; Hong, C. S. Fine-Tuning of the Carbon Dioxide Capture  
Capability of Diamine-Grafted Metal–Organic Framework Adsorbents  
Through Amine Functionalization. *ChemSusChem* **2017**, *10* (3),  
541–550.
- (57) Lee, W. R.; Kim, J. E.; Lee, S. J.; Kang, M.; Kang, D. W.; Lee,  
H. Y.; Hiremath, V.; Seo, J. G.; Jin, H.; Moon, D.; Cho, M.; Jung, Y.;  
Hong, C. S. Diamine-Functionalization of a Metal–Organic Frame-  
work Adsorbent for Superb Carbon Dioxide Adsorption and  
Desorption Properties. *ChemSusChem* **2018**, *11* (10), 1694–1707.
- (58) Kang, M.; Kim, J. E.; Kang, D. W.; Lee, H. Y.; Moon, D.; Hong,  
C. S. A Diamine-Grafted Metal–Organic Framework with Out-  
standing CO<sub>2</sub> Capture Properties and a Facile Coating Approach for  
Imparting Exceptional Moisture Stability. *J. Mater. Chem. A* **2019**, *7*  
(14), 8177–8183.
- (59) Hong, C. S.; Kang, M.; Kang, D. W. Post-Synthetic Diamine-  
Functionalization of MOF-74 Type Frameworks for Effective Carbon  
Dioxide Separation. *Dalton Trans* **2019**, *48*, 2263–2270.
- (60) Mosaic Materials, Inc., <http://mosaicmaterials.com/>.
- (61) Forse, A. C.; Milner, P. J.; Lee, J.-H.; Redfean, H. N.;  
Oktawiec, J.; Siegelman, R. L.; Martell, J. D.; Dinakar, B.; Porter-  
Zasada, L. B.; Gonzalez, M. I.; Neaton, J. B.; Long, J. R.; Reimer, J. A.  
Elucidating CO<sub>2</sub> Chemisorption in Diamine-Appended Metal–  
Organic Frameworks. *J. Am. Chem. Soc.* **2018**, *140* (51), 18016–  
18031.
- (62) NIST WebBook, <https://webbook.nist.gov/>.
- (63) Campbell, C. T.; Sellers, J. R. V. Enthalpies and Entropies of  
Adsorption on Well-Defined Oxide Surfaces: Experimental Measure-  
ments. *Chem. Rev.* **2013**, *113* (6), 4106–4135.
- (64) Bertani, P.; Raya, J.; Bechinger, B. <sup>15</sup>N Chemical Shift  
Referencing in Solid State NMR. *Solid State Nucl. Magn. Reson.*  
**2014**, *61–62*, 15–18.
- (65) Blöchl, P. E. Projector Augmented-Wave Method. *Phys. Rev. B:*  
*Condens. Matter Mater. Phys.* **1994**, *50* (24), 17953–17979.
- (66) Kresse, G.; Joubert, D. From Ultrasoft Pseudopotentials to the  
Projector Augmented-Wave Method. *Phys. Rev. B: Condens. Matter*  
*Mater. Phys.* **1999**, *59* (3), 1758–1775.
- (67) Kresse, G.; Hafner, J. Ab Initio Molecular Dynamics for Liquid  
Metals. *Phys. Rev. B: Condens. Matter Mater. Phys.* **1993**, *47* (1), 558–  
561.
- (68) Kresse, G.; Hafner, J. Ab Initio Molecular-Dynamics Simulation  
of the Liquid-Metal–Amorphous-Semiconductor Transition in  
Germanium. *Phys. Rev. B: Condens. Matter Mater. Phys.* **1994**, *49*  
(20), 14251–14269.
- (69) Kresse, G.; Furthmüller, J. Efficient Iterative Schemes for Ab  
Initio Total-Energy Calculations Using a Plane-Wave Basis Set. *Phys.*  
*Rev. B: Condens. Matter Mater. Phys.* **1996**, *54* (16), 11169–11186.
- (70) Kresse, G.; Furthmüller, J. Efficiency of Ab-Initio Total Energy  
Calculations for Metals and Semiconductors Using a Plane-Wave  
Basis Set. *Comput. Mater. Sci.* **1996**, *6* (1), 15–50.
- (71) Lee, K.; Murray, E. D.; Kong, L.; Lundqvist, B. I.; Langreth, D.  
C. Higher-Accuracy van Der Waals Density Functional. *Phys. Rev. B:*  
*Condens. Matter Mater. Phys.* **2010**, *82* (8), 081101.
- (72) Elsässer, C.; Fähnle, M.; Chan, C. T.; Ho, K. M. Density-  
functional Energies and Forces with Gaussian-Broadened Fractional  
Occupations. *Phys. Rev. B: Condens. Matter Mater. Phys.* **1994**, *49*  
(19), 13975–13978.
- (73) Baias, M.; Widdifield, C. M.; Dumez, J.-N.; Thompson, H. P.  
G.; Cooper, T. G.; Salager, E.; Bassil, S.; Stein, R. S.; Lesage, A.; Day,  
G. M.; Emsley, L. Powder Crystallography of Pharmaceutical  
Materials by Combined Crystal Structure Prediction and Solid-State

- 1385 <sup>1</sup>H NMR Spectroscopy. *Phys. Chem. Chem. Phys.* **2013**, *15* (21), 1386 8069–8080.
- 1387 (74) Ali, U.; Agbonghae, E. O.; Hughes, K. J.; Ingham, D. B.; Ma, L.; 1388 Pourkashanian, M. Techno-Economic Process Design of a Commercial-Scale Amine-Based CO<sub>2</sub> Capture System for Natural Gas 1389 Combined Cycle Power Plant with Exhaust Gas Recirculation. *Appl. Therm. Eng.* **2016**, *103*, 747–758.
- 1392 (75) Zhang, Z.; Yao, Z.-Z.; Xiang, S.; Chen, B. Perspective of 1393 Microporous Metal–Organic Frameworks for CO<sub>2</sub> Capture and 1394 Separation. *Energy Environ. Sci.* **2014**, *7* (9), 2868.
- 1395 (76) Sabouni, R.; Kazemian, H.; Rohani, S. Carbon Dioxide 1396 Capturing Technologies: A Review Focusing on Metal Organic 1397 Framework Materials (MOFs). *Environ. Sci. Pollut. Res.* **2014**, *21* (8), 1398 5427–5449.
- 1399 (77) Wang, Q.; Bai, J.; Lu, Z.; Pan, Y.; You, X. Finely Tuning MOFs 1400 towards High-Performance Post-Combustion CO<sub>2</sub> Capture Materials. 1401 *Chem. Commun.* **2016**, *52* (3), 443–452.
- 1402 (78) Yu, J.; Xie, L.-H.; Li, J.-R.; Ma, Y.; Seminario, J. M.; Balbuena, 1403 P. B. CO<sub>2</sub> Capture and Separations Using MOFs: Computational and 1404 Experimental Studies. *Chem. Rev.* **2017**, *117* (14), 9674–9754.
- 1405 (79) Alkhabbaz, M. A.; Bollini, P.; Foo, G. S.; Sievers, C.; Jones, C. 1406 W. Important Roles of Enthalpic and Entropic Contributions to CO<sub>2</sub> 1407 Capture from Simulated Flue Gas and Ambient Air Using 1408 Mesoporous Silica Grafted Amines. *J. Am. Chem. Soc.* **2014**, *136* 1409 (38), 13170–13173.
- 1410 (80) Xu, X.; Song, C.; Andresen, J. M.; Miller, B. G.; Scaroni, A. W. 1411 Novel Polyethylenimine-Modified Mesoporous Molecular Sieve of 1412 MCM-41 Type as High-Capacity Adsorbent for CO<sub>2</sub> Capture. *Energy Fuels* **2002**, *16* (6), 1463–1469.
- 1414 (81) Mason, J. A.; McDonald, T. M.; Bae, T.-H.; Bachman, J. E.; 1415 Sumida, K.; Dutton, J. J.; Kaye, S. S.; Long, J. R. Application of a 1416 High-Throughput Analyzer in Evaluating Solid Adsorbents for Post- 1417 Combustion Carbon Capture via Multicomponent Adsorption of 1418 CO<sub>2</sub>, N<sub>2</sub>, and H<sub>2</sub>O. *J. Am. Chem. Soc.* **2015**, *137* (14), 4787–4803.
- 1419 (82) Liao, P.-Q.; Chen, X.-W.; Liu, S.-Y.; Li, X.-Y.; Xu, Y.-T.; Tang, 1420 M.; Rui, Z.; Ji, H.; Zhang, J.-P.; Chen, X.-M. Putting an Ultrahigh 1421 Concentration of Amine Groups into a Metal–Organic Framework 1422 for CO<sub>2</sub> Capture at Low Pressures. *Chem. Sci.* **2016**, *7* (10), 6528– 1423 6533.
- 1424 (83) Bien, C. E.; Chen, K. K.; Chien, S.-C.; Reiner, B. R.; Lin, L.-C.; 1425 Wade, C. R.; Ho, W. S. W. Bioinspired Metal–Organic Framework 1426 for Trace CO<sub>2</sub> Capture. *J. Am. Chem. Soc.* **2018**, *140* (40), 12662– 1427 12666.
- 1428 (84) Darunte, L.; Sen, T.; Bhawanani, C.; Walton, K. S.; Sholl, D. S.; 1429 Realff, M. J.; Jones, C. W. Moving Beyond Adsorption Capacity in 1430 Design of Adsorbents for CO<sub>2</sub> Capture from Ultra-Dilute Feeds: 1431 Kinetics of CO<sub>2</sub> Adsorption in Materials with Stepped Isotherms. *Ind. Eng. Chem. Res.* **2019**, *58* (1), 366–377.
- 1433 (85) Zhang, W.; Shan, Y.; Seidel-Morgenstern, A. Breakthrough 1434 Curves and Elution Profiles of Single Solutes in Case of Adsorption 1435 Isotherms with Two Inflection Points. *J. Chromatogr. A* **2006**, *1107* 1436 (1–2), 216–225.
- 1437 (86) Helfferich, F. G.; Carr, P. W. Non-Linear Waves in 1438 Chromatography. *J. Chromatogr. A* **1993**, *629* (2), 97–122.
- 1439 (87) Golden, F. M. *Theory of Fixed-Bed Performance for Ion Exchange* 1440 *Accompanied by Chemical Reaction*; Ph.D. Thesis, University of 1441 California: Berkeley, CA, 1973.
- 1442 (88) Satyapal, S.; Filburn, T.; Trela, J.; Strange, J. Performance and 1443 Properties of a Solid Amine Sorbent for Carbon Dioxide Removal in 1444 Space Life Support Applications. *Energy Fuels* **2001**, *15* (2), 250–255.
- 1445 (89) Huang, H. Y.; Yang, R. T.; Chinn, D.; Munson, C. L. Amine- 1446 Grafted MCM-48 and Silica Xerogel as Superior Sorbents for Acidic 1447 Gas Removal from Natural Gas. *Ind. Eng. Chem. Res.* **2003**, *42* (12), 1448 2427–2433.
- 1449 (90) Xu, X.; Song, C.; Miller, B. G.; Scaroni, A. W. Influence of 1450 Moisture on CO<sub>2</sub> Separation from Gas Mixture by a Nanoporous 1451 Adsorbent Based on Polyethylenimine-Modified Molecular Sieve 1452 MCM-41. *Ind. Eng. Chem. Res.* **2005**, *44* (21), 8113–8119.
- (91) Serna-Guerrero, R.; Belmabkhout, Y.; Sayari, A. Further 1453 Investigations of CO<sub>2</sub> Capture Using Triamine-Grafted Pore- 1454 Expanded Mesoporous Silica. *Chem. Eng. J.* **2010**, *158* (3), 513–519. 1455
- (92) Serna-Guerrero, R.; Belmabkhout, Y.; Sayari, A. Triamine- 1456 Grafted Pore-Expanded Mesoporous Silica for CO<sub>2</sub> Capture: Effect of 1457 Moisture and Adsorbent Regeneration Strategies. *Adsorption* **2010**, *16* 1458 (6), 567–575. 1459
- (93) Goepfert, A.; Czaun, M.; May, R. B.; Prakash, G. K. S.; Olah, 1460 G. A.; Narayanan, S. R. Carbon Dioxide Capture from the Air Using a 1461 Polyamine Based Regenerable Solid Adsorbent. *J. Am. Chem. Soc.* **2011**, *133* (50), 20164–20167. 1462
- (94) Fan, Y.; Lively, R. P.; Labreche, Y.; Rezaei, F.; Koros, W. J.; 1463 Jones, C. W. Evaluation of CO<sub>2</sub> Adsorption Dynamics of Polymer/ 1464 Silica Supported Poly(ethylenimine) Hollow Fiber Sorbents in Rapid 1465 Temperature Swing Adsorption. *Int. J. Greenhouse Gas Control* **2014**, 1466 *21*, 61–71. 1467
- (95) Didas, S. A.; Sakwa-Novak, M. A.; Foo, G. S.; Sievers, C.; Jones, 1468 C. W. Effect of Amine Surface Coverage on the Co-Adsorption of 1469 CO<sub>2</sub> and Water: Spectral Deconvolution of Adsorbed Species. *J. Phys. Chem. Lett.* **2014**, *5* (23), 4194–4200. 1470
- (96) Hahn, M. W.; Steib, M.; Jentys, A.; Lercher, J. A. Mechanism 1471 and Kinetics of CO<sub>2</sub> Adsorption on Surface Bonded Amines. *J. Phys. Chem. C* **2015**, *119* (8), 4126–4135. 1472
- (97) Wang, D.; Wang, X.; Song, C. Comparative Study of Molecular 1473 Basket Sorbents Consisting of Polyallylamine and Polyethylenimine 1474 Functionalized SBA-15 for CO<sub>2</sub> Capture from Flue Gas. *ChemPhysChem* **2017**, *18* (22), 3163–3173. 1475
- (98) Zhang, H.; Goepfert, A.; Olah, G. A.; Prakash, G. K. S. 1476 Remarkable Effect of Moisture on the CO<sub>2</sub> Adsorption of Nano-Silica 1477 Supported Linear and Branched Polyethylenimine. *J. CO<sub>2</sub> Util.* **2017**, 1478 *19*, 91–99. 1479
- (99) Zhao, P.; Zhang, G.; Sun, Y.; Xu, Y. CO<sub>2</sub> Adsorption Behavior 1480 and Kinetics on Amine-Functionalized Composites Silica with 1481 Trimodal Nanoporous Structure. *Energy Fuels* **2017**, *31* (11), 1482 12508–12520. 1483
- (100) Leal, O.; Bolivar, C.; Ovalles, C.; García, J. J.; Espidel, Y. 1484 Reversible Adsorption of Carbon Dioxide on Amine Surface-Bonded 1485 Silica Gel. *Inorg. Chim. Acta* **1995**, *240* (1), 183–189. 1486
- (101) Chang, A. C. C.; Chuang, S. S. C.; Gray, M.; Soong, Y. In-Situ 1487 Infrared Study of CO<sub>2</sub> Adsorption on SBA-15 Grafted with  $\gamma$ - 1488 (Aminopropyl)Triethoxysilane. *Energy Fuels* **2003**, *17* (2), 468–473. 1489
- (102) Khatri, R. A.; Chuang, S. S. C.; Soong, Y.; Gray, M. Carbon 1490 Dioxide Capture by Diamine-Grafted SBA-15: A Combined Fourier 1491 Transform Infrared and Mass Spectrometry Study. *Ind. Eng. Chem. Res.* **2005**, *44* (10), 3702–3708. 1492
- (103) Moore, J. K.; Sakwa-Novak, M. A.; Chaikittisilp, W.; Mehta, A. 1493 K.; Conradi, M. S.; Jones, C. W.; Hayes, S. E. Characterization of a 1494 Mixture of CO<sub>2</sub> Adsorption Products in Hyperbranched Aminosilica 1495 Adsorbents by <sup>13</sup>C Solid-State NMR. *Environ. Sci. Technol.* **2015**, *49* 1496 (22), 13684–13691. 1497
- (104) Lee, J. J.; Chen, C.-H.; Shimon, D.; Hayes, S. E.; Sievers, C.; 1498 Jones, C. W. Effect of Humidity on the CO<sub>2</sub> Adsorption of Tertiary 1499 Amine Grafted SBA-15. *J. Phys. Chem. C* **2017**, *121* (42), 23480– 1500 23487. 1501
- (105) Yu, J.; Chuang, S. S. C. The Role of Water in CO<sub>2</sub> Capture by 1502 Amine. *Ind. Eng. Chem. Res.* **2017**, *56* (21), 6337–6347. 1503
- (106) Chen, C.-H.; Shimon, D.; Lee, J. J.; Didas, S. A.; Mehta, A. K.; 1504 Sievers, C.; Jones, C. W.; Hayes, S. E. Spectroscopic Characterization 1505 of Adsorbed <sup>13</sup>CO<sub>2</sub> on 3-Aminopropylsilyl-Modified SBA15 Meso- 1506 porous Silica. *Environ. Sci. Technol.* **2017**, *51* (11), 6553–6559. 1507
- (107) Yu, J.; Zhai, Y.; Chuang, S. S. C. Water-Enhancement in CO<sub>2</sub> 1508 Capture by Amines: An Insight into CO<sub>2</sub>-H<sub>2</sub>O Interactions on Amine 1509 Films and Sorbents. *Ind. Eng. Chem. Res.* **2018**, *57* (11), 4052–4062. 1510
- (108) Chen, C.-H.; Shimon, D.; Lee, J. J.; Mentink-Vigier, F.; Hung, 1511 I.; Sievers, C.; Jones, C. W.; Hayes, S. E. The “Missing” Bicarbonate in 1512 CO<sub>2</sub> Chemisorption Reactions on Solid Amine Sorbents. *J. Am. Chem. Soc.* **2018**, *140* (28), 8648–8651. 1513
- (109) Bacsik, Z.; Ahlsten, N.; Ziadi, A.; Zhao, G.; Garcia-Bennett, A. 1514 E.; Martín-Matute, B.; Hedin, N. Mechanisms and Kinetics for 1515



1522 Sorption of CO<sub>2</sub> on Bicontinuous Mesoporous Silica Modified with n-  
1523 Propylamine. *Langmuir* **2011**, *27* (17), 11118–11128.

1524 (110) Danon, A.; Stair, P. C.; Weitz, E. FTIR Study of CO<sub>2</sub>  
1525 Adsorption on Amine-Grafted SBA-15: Elucidation of Adsorbed  
1526 Species. *J. Phys. Chem. C* **2011**, *115* (23), 11540–11549.

1527 (111) Aziz, B.; Hedin, N.; Bacsik, Z. Quantification of  
1528 Chemisorption and Physisorption of Carbon Dioxide on Porous  
1529 Silica Modified by Propylamines: Effect of Amine Density. *Micro-  
1530 porous Mesoporous Mater.* **2012**, *159*, 42–49.

1531 (112) Mafrá, L.; Čendak, T.; Schneider, S.; Wiper, P. V.; Pires, J.;  
1532 Gomes, J. R. B.; Pinto, M. L. Structure of Chemisorbed CO<sub>2</sub> Species  
1533 in Amine-Functionalized Mesoporous Silicas Studied by Solid-State  
1534 NMR and Computer Modeling. *J. Am. Chem. Soc.* **2017**, *139* (1),  
1535 389–408.

1536 (113) Serna-Guerrero, R.; Da'na, E.; Sayari, A. New Insights into the  
1537 Interactions of CO<sub>2</sub> with Amine-Functionalized Silica. *Ind. Eng. Chem.  
1538 Res.* **2008**, *47* (23), 9406–9412.

1539 (114) Yu, J.; Chuang, S. S. C. The Structure of Adsorbed Species on  
1540 Immobilized Amines in CO<sub>2</sub> Capture: An in Situ IR Study. *Energy  
1541 Fuels* **2016**, *30* (9), 7579–7587.

1542 (115) Lee, J.-H.; Siegelman, R. L.; Maserati, L.; Rangel, T.; Helms,  
1543 B. A.; Long, J. R.; Neaton, J. B. Enhancement of CO<sub>2</sub> Binding and  
1544 Mechanical Properties upon Diamine Functionalization of  
1545 M<sub>2</sub>(dobpdc) Metal–Organic Frameworks. *Chem. Sci.* **2018**, *9* (23),  
1546 5197–5206.

1547 (116) Martell, J. D.; Porter-Zasada, L. B.; Forse, A. C.; Siegelman, R.  
1548 L.; Gonzalez, M. L.; Oktawiec, J.; Runčevski, T.; Xu, J.; Srebro-  
1549 Hooper, M.; Milner, P. J.; Colwell, K. A.; Autschbach, J.; Reimer, J.  
1550 A.; Long, J. R. Enantioselective Recognition of Ammonium  
1551 Carbamates in a Chiral Metal–Organic Framework. *J. Am. Chem.  
1552 Soc.* **2017**, *139* (44), 16000–16012.

1553 (117) Bollini, P.; Choi, S.; Drese, J. H.; Jones, C. W. Oxidative  
1554 Degradation of Aminosilica Adsorbents Relevant to Postcombustion  
1555 CO<sub>2</sub> Capture. *Energy Fuels* **2011**, *25* (5), 2416–2425.